Emerging Climate Signals in Oxygen Minimum Zones

Mathieu Delteil, Marina Lévy, Laurent Bopp

To cite this version:

Mathieu Delteil, Marina Lévy, Laurent Bopp. Emerging Climate Signals in Oxygen Minimum Zones. 2025. ⟨hal-05375503⟩

HAL Id: hal-05375503
https://cnrs.hal.science/hal-05375503v1
Preprint submitted on 20 Nov 2025

https://doi.org/10.5194/egusphere-2025-2805
Preprint. Discussion started: 23 July 2025

Emerging Climate Signals in Oxygen Minimum Zones

Mathieu Delteil[1], Marina Lévy[1], and Laurent Bopp[2]
[1]Laboratoire d'Océanographie et du Climat, Sorbonne Université, Institut Pierre Simon Laplace (LOCEAN, SU/CNRS/IRD/MNHN), 75252 Paris CEDEX 05, France
[2]LMD-IPSL, Ecole Normale Supérieure – Université PSL, CNRS, École Polytechnique, Sorbonne Université, Paris, France
Correspondence: Mathieu Delteil (mathieu.delteil@locean.ipsl.fr)

Abstract.

The ocean is losing oxygen due to anthropogenic climate change. This loss is particularly worrying when it occurs in naturally low-oxygen regions, such as the Oxygen Minimum Zones (OMZs) found at mid-depth in tropical oceans, because the expansion of OMZs reduces habitable space for marine life and threatens oxygen-dependent ecosystems. However, detecting the emergence of climate-driven signals is challenging due to internal variability. Here, we isolate externally forced signals of OMZ volume change and regional deoxygenation, and determine their time of emergence using the IPSL-CM6A-LR Large Ensemble. We apply time of emergence analysis to identify when climate-driven signals become statistically distinguishable from natural variability. Our results show that OMZ edges consistently expand, with emergence occurring in the second half of the 20th century, which is in phase with regional mean deoxygenation in the tropical Pacific and tropical Atlantic. In contrast, we reveal a marked spatial asymmetry in the emergence of OMZ core and hypoxic volumes between the northern and southern parts of OMZs. While OMZ core volumes in the tropical North Pacific and hypoxic volumes in the tropical North Atlantic expand, their southern counterparts contract due to a sudden, ventilation-driven oxygen increase from the Southern Ocean at the start of the 21st century. Uncertainties in emergence timing range from 20 to 30 years across ensemble members, and increase substantially in regions influenced by abrupt changes in OMZ ventilation. By linking the emergence of regional deoxygenation to that of OMZ volume changes, climate-driven expansions of OMZ volumes are likely already beginning to emerge, with distinct dynamics between northern and southern tropical oceans.

1 Introduction

The global ocean is losing oxygen as a consequence of climate warming, with historical observations indicating a ∼ 2 % global decline in oxygen concentrations over the past 50 years (Keeling et al., 2010; Schmidtko et al., 2017; Ito et al., 2017). Ocean deoxygenation poses a direct threat to aerobic organisms and marine ecosystems (Stramma et al., 2012; Vaquer-Sunyer and Duarte, 2008). Although the distribution of dissolved oxygen is highly heterogeneous in the ocean, oxygen declines have been recorded in both well-oxygenated regions and in areas where concentrations are already critically low, the latter known as Oxygen Minimum Zones (OMZ) (Schmidtko et al., 2017; Ito et al., 2017). OMZs are typically located in poorly ventilated regions of the ocean and beneath zones of high biological productivity, where oxygen consumption is elevated (Luyten et al., 1983; Paulmier and Ruiz-Pino, 2009). Consequently, OMZs are found mainly at intermediate depths (∼ 100 to 1000m deep) in tropical regions. The largest OMZ is located in the tropical Pacific Ocean, with additional major OMZs in the tropical Atlantic and the North Indian Ocean.

OMZs are regions of the ocean in which dissolved oxygen concentrations fall below the hypoxic threshold, posing a threat to oxygen-dependent marine life (Stramma et al., 2008). In their core, oxygen levels can drop even further, sometimes below anoxic thresholds (Stramma et al., 2008). Although deoxygenation rates tend to be lower in these already hypoxic areas compared to better ventilated regions, ongoing oxygen loss can lead to expansion of OMZs (Stramma et al., 2008; Deutsch et al., 2014; Ito et al., 2017; Levin, 2018). This potential increase in the volume of OMZ is a critical concern, as it could significantly reduce the habitable space available to marine ecosystems (Stramma et al., 2012; Levin, 2018). Therefore, it is essential to assess future levels of deoxygenation along with changes in OMZ volume, as both factors combine to determine the extent and severity of low-oxygen habitats. However, it remains challenging to track long-term volume changes directly from observations due to sparse spatial coverage and limited time series; this makes Earth System Models essential for identifying large-scale patterns and anticipating future changes.

Although there is strong evidence that ocean deoxygenation will continue to intensify in response to climate change, projections of future OMZ volume changes remain highly uncertain (Resplandy, 2018; Bahl et al., 2019; Kwiatkowski et al., 2020; Lévy et al., 2022). OMZ volume changes are governed by the balance between water mass ventilation and biological oxygen consumption (Resplandy, 2018), and this balance is not consistently represented in coarse-resolution ESMs (Lévy et al., 2022). A key source of uncertainty lies in the parametrisation of mixing, which directly affects oxygen supply through ventilation and indirectly impacts oxygen consumption through biological processes (Duteil and Oschlies, 2011; Bahl et al., 2019). For these reasons, previous studies based on Earth System Models (ESM) from the Phase 5 of the Coupled Model Intercomparison Project (CMIP5, Taylor et al. (2012)) failed to reach consensus on OMZ expansion or contraction, particularly in the tropics (Bopp et al., 2013; Cabré et al., 2015).

Shifting the analysis of OMZ evolution from a geographic-space to an oxygen-space framework helped reconcile apparent discrepancies in projections across models (Ditkovsky and Resplandy, 2025). Within this oxygen framework, OMZ projections from the Coupled Model Intercomparison Project Phase 6 (CMIP6, Eyring et al. (2016)) could be coherently categorized into three distinct regimes: the OMZ core, projected to shrink; hypoxic waters, which represent a transitional regime with uncertain future trends; and low-oxygen waters, projected to expand due to reduced ventilation (Busecke et al., 2022; Ditkovsky et al., 2023). This categorisation helped reduce the spread among CMIP6 model projections.

Despite statistically significant trends in OMZ volumes identified using CMIP6 models (Busecke et al., 2022; Ditkovsky et al., 2023), attributing these trends to externally forced climate change remains challenging due to strong internal variability (Ito and Deutsch, 2010; Poupon et al., 2023). This internal variability is a natural and intrinsic dynamics of the coupled model, arising from non linear natural dynamical processes and interactions among climate system components (Lorenz, 1963; Hasselmann, 1976). For a forced signal to be detectable, it must rise above this background noise (Hasselmann, 1993; Santer et al., 1994). The detectability thus becomes a signal-to-noise ratio problem, where emergence occurs once the magnitude and persistence of the externally forced trend exceed the envelope of internal variability (Hasselmann, 1993; Santer et al., 1994). This notion of emergence is crucial, as it marks the point at which climate-driven changes can be confidently separated from internal variability and thus the moment when oxygen concentrations are forced beyond natural conditions experienced by marine ecosystems.

However, when performing a single simulation using an Earth System Model, externally-forced (natural and anthropogenic) changes of deoxygenation and OMZ volumes are intertwined with internal variability (Deser et al., 2012). Although the climate-driven signal is often approximated by a linear trend, this method fails to capture the non-linearity of external forcing. Consequently, it inaccurately represents the amplitude of long-term changes, while also misrepresenting the amplitude and phase of the estimated internal variability (Mann, 2008; Frankcombe et al., 2015).

To overcome these limitations, Large Ensembles, consisting of multiple simulations performed with the same Earth System Model, are essential to isolate forced climate signals from internal variability. With a sufficiently large number of simulations, the spread arises purely from internal variability, and the climate-driven signal can be isolated through ensemble averaging (Deser et al., 2012).

In this study, we pursue two main objectives: extract climate-driven changes in ocean deoxygenation and OMZ volumes, and assess the time at which these signals emerge from internal variability. In doing so, we aim to bridge the gap between what can currently be observed and what might be detectable in the future, by using models to explore when that change becomes or has become distinguishable from natural variability.

We conduct a regional analysis across five key OMZ regions to assess co-evolution of deoxygenation and OMZ volumes under ocean warming: the tropical North Pacific, tropical South Pacific, tropical North Atlantic, tropical South Atlantic, and North Indian Ocean. We track the evolution of dissolved oxygen and OMZ volumes using the oxygen-space framework developed by Ditkovsky and Resplandy (2025). Following the regimes identified by Ditkovsky et al. (2023), we distinguish three OMZ volume classes: OMZ Core volumes ($[O_2] < 20\text{µmol.kg}^{-1}$), where nitrous oxide is produced (Ji et al., 2015); Hypoxic volumes ($[O_2] < 60\text{µmol.kg}^{-1}$), which are harmful to many marine organisms (Miller et al., 2002; Vaquer-Sunyer and Duarte, 2008); and Low-oxygen volumes ($[O_2] < 120\text{µmol.kg}^{-1}$), which influence the distribution of marine ecosystems (Bertrand et al., 2011). To isolate the externally forced climate signal, we leverage the IPSL-CM6A-LR Large Ensemble (Bonnet et al., 2021), which consists of 32 ensemble members. The IPSL-CM6A-LR Large Ensemble has already proven effective in extracting the anthropogenic component of ocean warming (Silvy et al., 2022). We apply the concept of time of emergence, which quantifies when the forced climate signal becomes distinguishable from internal variability (Hawkins and Sutton, 2012). Previous studies have used this method to detect the emergence of deoxygenation at the global scale (Long et al., 2016; Hameau et al., 2019), in regional basins (Gong et al., 2021), and at various depths (Gong et al., 2021). While these studies focused on oxygen concentrations, we extend the method to OMZ volume metrics, providing a complementary perspective on the detectability of low-oxygen changes under climate forcing.

Our findings reveal that OMZ volumes in the tropical North Pacific and tropical North Atlantic expand and their climate-driven signals emerge from internal variability before the early 21st century in the IPSL model. The deoxygenation signal appears concurrently with the expansion of Low-oxygen OMZ volumes, defined by higher oxygen thresholds within the OMZ range, indicating that deoxygenation serves as an indicator of OMZ volume expansion. We also highlight a pronounced North–South asymmetry in OMZ Core dynamics. In the tropical North Pacific and tropical North Atlantic, the most oxygen-

https://doi.org/10.5194/egusphere-2025-2805
Preprint. Discussion started: 23 July 2025

depleted volumes expand. In contrast, in the tropical South Pacific and tropical South Atlantic, extratropical ventilation plays a key role by actively driving a contraction of the most oxygen-depleted volumes. In these Southern OMZ regions, the OMZ Core volumes do not emerge from internal variability before the mid-21st century in the IPSL simulations.

2 Materials and methods

2.1 Model and simulations

2.1.1 IPSL-CM6A-LR description

The model used for this study is the IPSL-CM6A-LR (Boucher et al., 2020), an Earth System Model (ESM) developed by the Institut Pierre Simon Laplace (IPSL). The model was one of the models used in of the sixth phase of the Coupled Model Intercomparaison Project (CMIP6, Eyring et al. (2016)). It couples three modules : the LMDZ atmospheric model version 6A-LR (Hourdin et al., 2020), the ORCHIDEE land surface model version 2.0 (Krinner et al., 2005) and the NEMO oceanic model version 3.6 (Madec et al., 2017). The ocean module of the model includes three major components: the ocean physics NEMO-OPA (Madec et al., 2017), the sea ice dynamics and thermodynamics NEMO-LIM3 (Rousset et al., 2015; Vancoppenolle et al., 2009), and the ocean biogeochemistry NEMO-PISCES (Aumont et al., 2015).
The atmospheric module uses a $2.5°$x$1.3°$ horizontal resolution and 79 vertical levels. The oceanic module uses the eORCA1 configuration which is a tripolar grid with a $1°$ nominal resolution and a refinement at $1/3°$ in the equatorial region. The eORCA1 grid has 75 vertical levels.
The O_2 concentrations are used in the model in $\mathrm{mmol.m^{-3}}$ and are subsequently converted to $\mathrm{\mu mol.kg^{-1}}$ using a constant reference density of $\rho_0 = 1,025\mathrm{kg.m^{-3}}$.

2.1.2 IPSL-CM6A-LR Large Ensemble

This study uses the Large Ensemble of the IPSL-CM6A-LR model. The Large Ensemble consists of a piControl simulation and 32 historical-EXT experiences (Bonnet et al., 2021). The piControl run is a 2000 years control simulation using pre-industrial climate forcing. The historical-EXT simulations are initialised from different years of the piControl and run for 210 years (Figure 1a). Initialisation conditions of historical-EXT are picked out from the piControl experiment every 20 to 40 years so that the ensemble samples the phases of the low-frequency variability present in the model (Bonnet et al., 2021). Thus, initialisations of historical-EXT occur between the 20th and the 830th year of piControl simulation time. All of the historical-EXT are run under the CMIP6 historical procedure during 164 years (1850-2014) and then extended from 2015 to 2060 using radiative forcing of the SSP2-4.5 scenario, except for the ozone field which has been kept constant to its 2014 climatology (O'Neill et al., 2016; Bonnet et al., 2021). Due to file corruption, member r2i1p1f1 and member r16i1p1f1 were rejected then only 30 members were considered.
Each member of the IPSL-CM6A-LR contains both the climate-driven signal and some internal variability of the climate system. Large ensembles are useful tools to isolate these two components. By averaging across multiple members, defining the

https://doi.org/10.5194/egusphere-2025-2805
Preprint. Discussion started: 23 July 2025

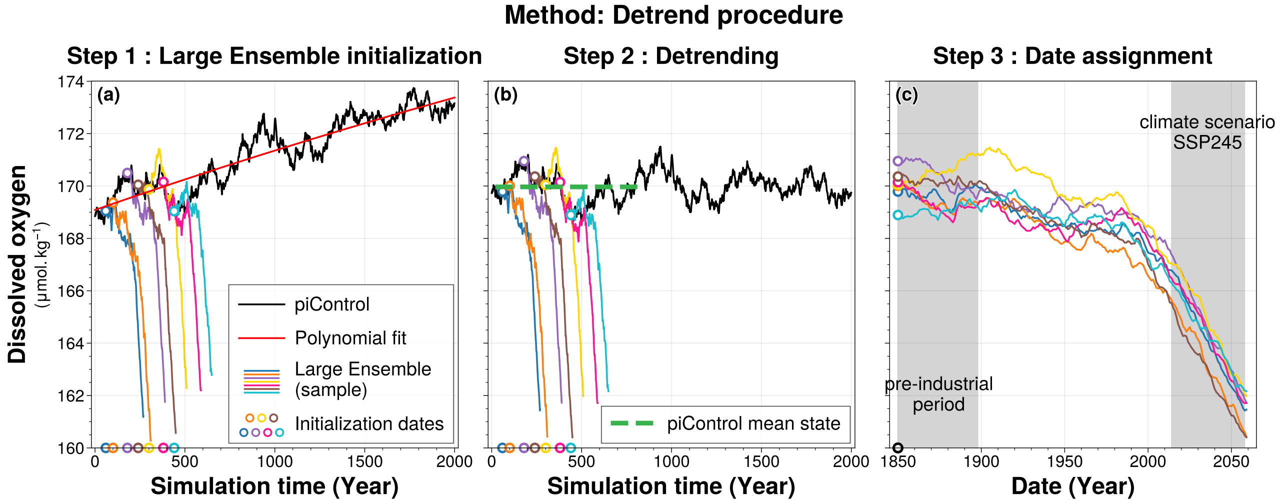

Figure 1. Detrend procedure for global ocean mean of dissolved oxygen concentration between $100-1000\mathrm{m}$ depth. Time series from the piControl simulation are shown in **black** in both panels **(a)** and **(b)**. In all three panels, **coloured lines** represent a subset of 7 ensemble members (out of the 30) from the historical-EXT simulation of the IPSL-CM6A-LR model : members 1, 4, 6, 9, 11, 17, and 22. The starting points of each member are marked by **coloured rings**, with the ring colours corresponding to the respective lines. Panel **(a)** shows the raw data, with the millennial polynomial drift from the piControl simulation in **red**. Panel **(b)** shows the detrended data, with the **green line** indicating the piControl mean state over the simulation period 20-830. Panel **(c)** shows the historical-EXT ensemble members shifted to the simulation forcing years, 1850-2059.

Large Ensemble inter-member mean, the forced signal is extracted from the internal variability of the climate system. Internal variability can thus be estimated by the inter-member spread, measured by its standard deviation (Deser et al., 2012).

2.1.3 Model drift correction

The piControl simulation in IPSL-CM6A-LR has a quasi-linear cooling drift in global mean ocean temperature, originating from a mean net surface heat loss (Mignot et al., 2021). This drift propagates into the historical simulations and onto the oxygen concentration evolution. To correct for this drift, we followed the methodology of Silvy et al. (2022). While the method is applied at each grid point, Figure 1 illustrates its implementation using the global mean oxygen concentration over the 100˘1000m depth range for clarity. We fitted a second order polynomial to the 2000-yr piControl annual means (Figure 1a). Using the full piControl period ensures that the drift is isolated, preventing the capture of low-frequency internal variability (Gupta et al., 2013). We then subtracted the corresponding 210-year segment of this polynomial fit from each ensemble member, aligning with its respective piControl period, and subsequently added the same mean state back to each member (Figure 1b). This mean state is defined as the mean of the piControl calculated over the period when the historical-extended simulations were performed, spanning simulation years 20 to 830 of piControl simulation. By adding this mean state, we preserve absolute oxygen concentrations rather than anomalies.

https://doi.org/10.5194/egusphere-2025-2805
Preprint. Discussion started: 23 July 2025

After this correction, the spread across all 30 members reflects only differences in phasing of internal variability, as their mean states are no longer shifted by their initialisation in the drifting piControl. Consequently, the IPSL-CM6A-LR Large Ensemble consists of 30 historical-EXT simulations, all forced by the same historical and SSP2-4.5 climate scenario, with variations arising purely from differences in the phasing of internal variability dictated by their initial conditions (Figure 1c).

2.2 Model evaluation

Here, we evaluate the representation of dissolved oxygen content and deoxygenation trends in the IPSL-CM6A-LR Large Ensemble simulations (Figures 2 and 3).

2.2.1 Datasets

We use oxygen data from the World Ocean Atlas 2018 (WOA18, García et al. (2018)) to evaluate the oxygen content in the IPSL-CM6A-LR Large Ensemble simulations. WOA18 provides an objectively analysed climatology of in situ dissolved oxygen measurements, offering a robust reference for large-scale oceanic oxygen distributions.

To evaluate present-day oxygen trends (1970–2014) in the IPSL-CM6A-LR Large Ensemble, we use the Institute of Atmospheric Physics (IAP) dataset from the Chinese Academy of Sciences (Cheng and Gouretski, 2023). This time-dependent dataset integrates observations from CTD, Argo floats, and bottle samples. To correct biases in Argo measurements, Cheng and Gouretski (2023) applied quality control procedures from Gouretski et al. (2024) and interpolated the data onto a 1 degree grid using the method described in (Cheng and Zhu, 2016).

Additionally, we evaluate the performance of the IPSL-CM6A-LR model by comparing it against outputs from 10 other Earth System Models (ESMs) that participated in the CMIP6 project (Eyring et al., 2016). The selection of the models was based on the availability of dissolved oxygen variable necessary to evaluate IPSL-CM6A-LR model. The models are ACCESS-ESM1-5 (Ziehn et al., 2020), CanESM5 (Swart et al., 2019), CNRM-ESM2-1 (Séférian et al., 2019), GFDL-CM4 (Held et al., 2019), GFDL-ESM4 (Dunne et al., 2020; Stock et al., 2020), MIROC-ES2L (Hajima et al., 2020), MPI-ESM1-2-HR (Müller et al., 2018; Mauritsen et al., 2019), MRI-ESM2-0 (Yukimoto et al., 2019), NorESM2-LM (Tjiputra et al., 2020), and UKESM1-0-LL (Sellar et al., 2019). All models are assessed over the present-day period (1970–2014) following the CMIP6 historical protocol and over climate change scenario period (2015-2059) following the SSP2-4.5 scenario protocol (O'Neill et al., 2016). The analysis focuses on the $100-1000\mathrm{m}$ depth range, and results from individual models are averaged to compute the CMIP6 multi-model mean.

2.2.2 Model evaluation of oxygen

In this section, we evaluate the present-day (1970–2014) dissolved oxygen climatology in IPSL-CM6A-LR against observations from WOA18 and other CMIP6 models. Specifically, we compare the present-day climatologies of WOA18 and the CMIP6 multi-model mean with the inter-member mean climatology of the IPSL-CM6A-LR Large Ensemble over the same period (Figure 2). All climatologies are computed at fixed depths, between 100 and $1000\mathrm{m}$.

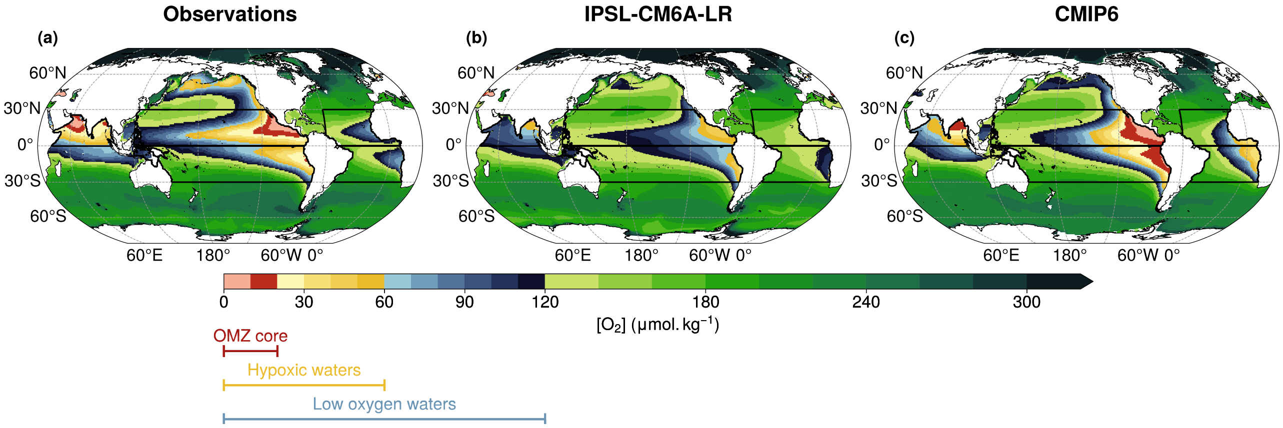

Figure 2. Vertical mean dissolved oxygen concentration between $100-1000$m for the present-day period (1970-2014) climatology, using **(a)** the World Ocean Atlas 2018 dataset, **(b)** the IPSL-CM6A-LR Large Ensemble inter-member mean, and **(c)** the CMIP6 multi-model ensemble mean. The colourbar indicates oxygen concentration boundaries: **(red)** OMZ core below 20µmol.kg^{-1}, **(yellow)** hypoxic waters below 60µmol.kg^{-1} and **(blue)** low-oxygen waters below 120µmol.kg^{-1}. In all panels, the **black boxes** represent the five domains considered in this study.

We focus on the representation of three key oxygen concentration thresholds, which are critical for climate and marine ecosystems (Figure 2): oxygen concentrations below 20µmol.kg^{-1}, corresponding to the Core of the Oxygen Minimum Zones; oxygen concentrations below 60µmol.kg^{-1}, defining Hypoxic waters; oxygen concentrations below 120µmol.kg^{-1}, representing Low-oxygen waters.

The IPSL-CM6A-LR model shows an oxygen surplus (Figure 2b), resulting in a misrepresentation of oxygen concentrations (Aumont et al., 2015). While the model provides a better representation of Low-oxygen waters compared to Hypoxic waters and OMZ Cores, it still significantly underestimates Hypoxic waters and fails to capture the OMZ Cores (Figure 2b). In the tropical North Pacific and North Indian Ocean, observations reveal well-defined OMZ Core waters, which are absent in the simulation (Figure 2a and b). In the North Indian Ocean, the IPSL climatology shows an oxygen minimum in the Bay of Bengal (Figure 2b) but fails to represent Hypoxic waters and OMZ Core in the Arabian Sea, both of which are present in observations (Figure 2a and b). As a result, in the North Indian Ocean, the IPSL Hypoxic waters account for only 10% of the observed Hypoxic waters. In the tropical Pacific, Hypoxic waters are also significantly underestimated, representing 24% of the observed volume in the tropical North Pacific and 42% in the tropical South Pacific (Figure 2a and b). The oxygen underestimation in the tropical Pacific is likely linked to an underestimation of nutrients, possibly due to a weaker Equatorial Undercurrent (Cabré et al., 2015). However, the IPSL model successfully captures the north-south structure of the tropical Pacific Hypoxic waters (Figure 2a and b). A key feature of this structure is the higher dissolved oxygen concentrations along the Equator, compared to lower concentrations on either side, leading to the equatorial separation of the OMZ Core (Busecke et al., 2022). In contrast, it fails to reproduce the Low-oxygen waters structure in the tropical Atlantic basin, where only the

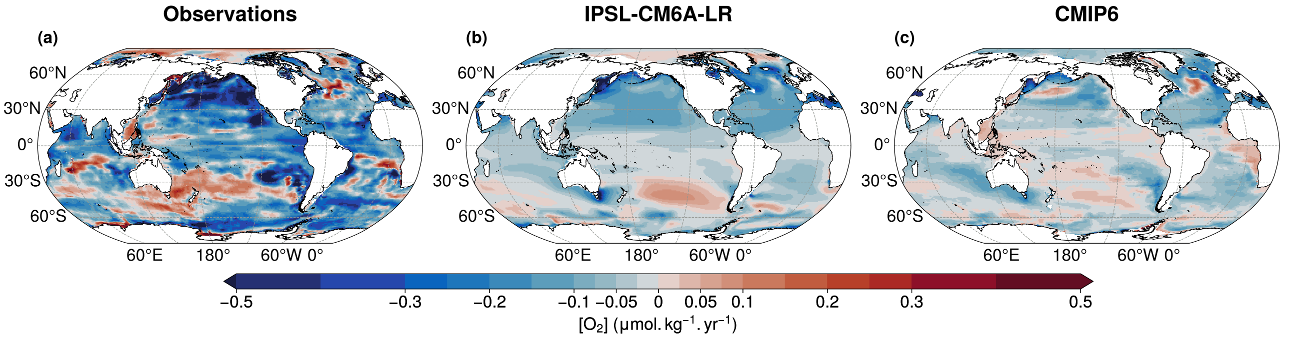

Figure 3. Vertical mean dissolved oxygen trends between $100-1000\mathrm{m}$ for the present-day period (1970-2014), using **(a)** the Cheng and Gouretski (2023) dataset, **(b)** the IPSL-CM6A-LR Large Ensemble inter-member mean, and **(c)** the CMIP6 multi-model ensemble mean. In all panels, **black boxes** represent the five domains considered in this study.

tropical South Atlantic Low-oxygen waters are simulated (Figure 2b). Across all regions, the IPSL simulations systematically overestimate oxygen concentrations compared to observations (Figure 2a).

The misrepresentation of dissolved oxygen is not unique to IPSL-CM6A-LR model. It is also present in the CMIP6 multi-model climatology (Figure 2c). Like IPSL, CMIP6 models fail to capture OMZ core waters in the North Indian Ocean, with an oxygen minimum in the Arabian Sea rather than in the Bay of Bengal. However, in the tropical North Pacific and tropical North Atlantic, CMIP6 models better represent Low-oxygen waters (Figure 2c). OMZ core waters are present in the tropical North Pacific in the CMIP6 mean. In contrast, in the tropical South Pacific and tropical South Atlantic, CMIP6 models underestimate dissolved oxygen. Overall, the IPSL-CM6A-LR climatology simulates higher oxygen levels than the CMIP6 multi-model mean.

2.2.3 Model evaluation of deoxygenation

In this section, we evaluate trends in dissolved oxygen in the IPSL-CM6A-LR Large Ensemble inter-member mean by comparing them with observations from the Institute of Atmospheric Physics dataset (Cheng and Gouretski, 2023) and other CMIP6 models (Figure 3). These trends are computed over a fixed depth range between 100 and $1000\mathrm{m}$ using ordinary least-squares linear regression for all datasets (Storch and Swiers, 1999). A 90% confidence interval is applied, accounting for the reduction in degrees of freedom (Storch and Swiers, 1999).

Firstly, we examine present-day trends over the period 1970–2014. All members of the IPSL Large Ensemble exhibit a global decline in oceanic dissolved oxygen. The ensemble mean shows a decrease of -1.25% in global mean oxygen concentration, which is greater than the decline of -0.95% showed by the CMIP6 multi-model mean. However, both IPSL Large Ensemble and CMIP6 multi-model underestimate the observed oxygen decline. The IAP dataset shows a reduction of -2.83% over the present day period. This underestimation is also reflected in the linear trends of deoxygenation. The IPSL Large Ensemble simulates a global mean deoxygenation rate of $-0.053\pm0.023\mathrm{\mu mol.kg^{-1}.yr^{-1}}$, exceeding the CMIP6 multi-model mean rate

https://doi.org/10.5194/egusphere-2025-2805
Preprint. Discussion started: 23 July 2025

of $-0.036 \pm 0.022\mu\mathrm{mol.kg}^{-1}.\mathrm{yr}^{-1}$, yet still considerably lower than the observed trend of $-0.132 \pm 0.097\mu\mathrm{mol.kg}^{-1}.\mathrm{yr}^{-1}$ from the IAP dataset.

The IPSL-CM6A-LR Large Ensemble mean and CMIP6 multi-model mean show a spatial distribution of present-day deoxygenation that is consistent with IAP observation dataset (Figure 3). Both IPSL Large Ensemble and CMIP6 multi-model show stronger deoxygenation rates at high latitudes, in agreement with the IAP dataset (Figure 3). However, regional trends in the models are weaker than those observed (Figure 3). Observations indicate significant oxygenation in the Southern Hemisphere, particularly in the South Pacific and South Indian Oceans (Figure 3a). The IPSL Large Ensemble captures this oxygenation trend in both regions (Figure 3b). The tropical Pacific shows deoxygenation in both observations and IPSL simulations (Figure 3a, b). In the Atlantic basin, IPSL simulations shows widespread deoxygenation but fails to reproduce regional oxygenation trends. Both the IAP dataset and the CMIP6 multi-model mean capture oxygenation in the North Atlantic and the Benguela upwelling system (Figure 3). Similarly, in the North Indian Ocean, IPSL simulations fail to reproduce the observed dipole of oxygenation and deoxygenation, which is well represented in both the IAP dataset and the CMIP6 multi-model mean (Figure 3).

Then, we assess future trends under SSP2-4.5 climate scenario forcing over the period 2015–2059. The IPSL-CM6A-LR Large Ensemble inter-member mean shows a stronger deoxygenation trend than during the present-day period, with a global mean oxygen decline of $-0.1139 \pm 0.0027\mu\mathrm{mol.kg}^{-1}.\mathrm{yr}^{-1}$. All historical-EXT members of the IPSL Large Ensemble show deoxygenation trends under the SSP2-4.5 scenario, consistent with the ensemble mean (Figure 1c). The IPSL-simulated deoxygenation rate is higher than CMIP6 multi-model projections, as the CMIP6 multi-model mean shows a global oxygen decline of $-0.0536 \pm 0.0041\mu\mathrm{mol.kg}^{-1}.\mathrm{yr}^{-1}$.

2.3 Deoxygenation and OMZ metrics

To investigate the response of OMZs to ongoing ocean deoxygenation, both phenomena need to be tracked within consistent spatial domains. This approach enables a direct comparison between OMZ dynamics and its corresponding regional deoxygenation trends. We define five fixed regional boxes corresponding to the major OMZs (Figure 2, 5): tropical North Pacific (0°S-30°N/120°E-295°E), tropical South Pacific (30°S-0°N/120°E-295°E), tropical North Atlantic (0°S-30°N/60°W-20°E), tropical South Atlantic (30°S-0°N/60°W-20°E) and North Indian (0°S-30°N/35°E-120°E). We also restrict our analysis to the $100-1000\mathrm{m}$ depth range, where dissolved oxygen concentrations are at their lowest.

Ocean deoxygenation is quantified by tracking temporal trends in spatially averaged, both vertical and horizontal, dissolved oxygen concentrations within each box.

OMZ metrics are commonly defined in the geographic space as the ocean volume with oxygen concentration below a certain threshold (Busecke et al., 2022). However, as demonstrated in the model evaluation, the IPSL-CM6A-LR Large Ensemble does not accurately reproduce the observed locations and extent of OMZ Core waters, Hypoxic waters and Low-oxygen waters, limiting the relevance of analysing OMZ changes in the geographic space (Figure 2). To overcome this limitation, we adopt the "ventilation-space" approach developed by Ditkovsky and Resplandy (2025), based on the "oxygen water mass framework".

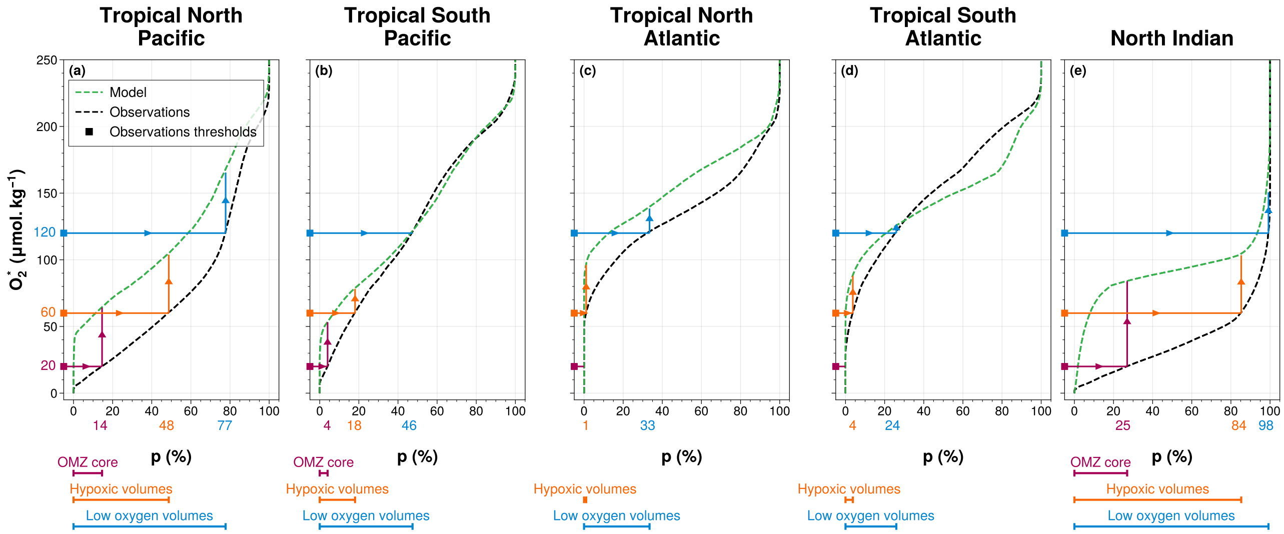

Figure 4. OMZ volume definition in IPSL-CM6A-LR simulations. For each of the five OMZ spatial boxes, the volume percentile p is computed as a function of O_2 threshold using **(black dashed lines)** the World Ocean Atlas database and **(green dashed lines)** the IPSL-CM6A-LR Large Ensemble inter-member mean. The three thresholds (**(purple)** 20µmol.kg^{-1}, **(orange)** 60µmol.kg^{-1} and **(blue)** 120µmol.kg^{-1}) define **(coloured bands)** the three volume percentiles of interest for each OMZ spatial box in WOA: **(purple)** OMZ Core, **(orange)** Hypoxic volumes and **(blue)** Low-oxygen volumes (Table 1). These percentiles are then used to compute the corresponding OMZ volumes in the IPSL-CM6A-LR simulations **(arrowed lines)**.

In this framework, water masses are characterised by the oxygen-percentile relation $O_2^*(p,t)$ (Ditkovsky and Resplandy, 2025). The oxygen-percentile p represents the proportion of ocean volume with oxygen concentrations below O_2^* at time t, computed as (Sohail et al., 2021; Ditkovsky and Resplandy, 2025),

$$p(O_2^*,t) = 100 * \mathcal{V}(O_2^*,t)/\mathcal{V}_T \tag{1}$$

with $\mathcal{V}_T$ being the total volume considered and $\mathcal{V}(O_2^*,t)$ is defined as:

$$\mathcal{V}(O_2^*,t) = \iiint\limits_{O_2(x,y,z,t)<O_2^*} dV \tag{2}$$

The oxygen-percentile relations are computed using both the WOA18 climatology and the IPSL-CM6A-LR inter-member mean averaged over the present day period (1970-2014) (Figure 4). It is computed within each of the five OMZ regions (Figure 4). The IPSL model captures the overall shape of the oxygen–percentile relation observed in the WOA18 dataset (Figure 4), although it generally overestimates oxygen concentrations. Consequently, for a given percentile, the model corresponds to a higher oxygen threshold, except in the tropical South Pacific and tropical South Atlantic. In the former, a positive bias is observed below the 47th percentile; in the latter, a positive bias appears below the 29st percentile and a negative bias above it (Figure 4). These biases are consistent with the model oxygen content surplus and spatial mismatches previously described.

https://doi.org/10.5194/egusphere-2025-2805
Preprint. Discussion started: 23 July 2025

Table 1. Volume percentile of interest in the IPSL-CM6A-LR Large Ensemble inter-member mean for each OMZ spatial box, computed as fraction (%) of the total volume of respective OMZ spatial box.

	Tropical Pacific	Tropical South Pacific	Tropical North Atlantic	Tropical South Atlantic	North Indian
OMZ Core	14	4	-	-	25
Hypoxic volumes	48	18	1	4	84
Low-oxygen volumes	77	46	33	24	98

To account for these systematic biases, we define OMZ volumes in "ventilation-space" using percentile thresholds derived from WOA18 (Ditkovsky and Resplandy, 2025). In each region, we identify the percentile corresponding to three key oxygen thresholds in the WOA18 climatology: 20µmol.kg^{-1} for OMZ Core waters; 60µmol.kg^{-1} for Hypoxic waters; and 120µmol.kg^{-1} for Low-oxygen waters. In the Atlantic basin, oxygen concentrations in observations do not fall below 20µmol.kg^{-1}; therefore, the OMZ Core is not defined in the tropical North and South Atlantic (Figure 4). The percentiles associated with these thresholds are then applied to the IPSL oxygen–percentile curves, allowing consistent identification of the three OMZ volume categories in both observations and simulations (Figure 4, Table 1). This method enables us to track the evolution of OMZ volumes and their oxygen content over time while taking into account the model's oxygen biases.

We further analyse the spatial distribution of OMZ volumes defined in "ventilation-space" (Figure 5). Across all OMZ volume classes, the thickest areas of OMZ volumes in the IPSL simulations align with those observed in WOA18. However, in observations, OMZ thickness decreases sharply at their boundaries with sharp oxygen concentration gradient, whereas in the IPSL Large Ensemble mean, the transition is more gradual, resulting in more extensive OMZ volumes (Figure 5). Additionally, the North Indian OMZ volumes in the model are predominantly located in the Bay of Bengal, whereas observations indicate a signal both in the Arabian Sea and the Bay of Bengal (Figure 5).

2.4 Oxygen decomposition

To investigate the drivers of deoxygenation within the selected OMZ spatial boxes, we decompose changes in dissolved oxygen (O_2) concentrations into two components: the saturation concentration of oxygen ($O_{2,sat}$) and the Apparent Oxygen Utilisation (AOU). This decomposition follows:

$$\Delta O_2 = \Delta O_{2,sat} - \Delta AOU \tag{3}$$

The saturation concentration $O_{2,sat}$ represents the oxygen solubility, which depends non-linearly on temperature and salinity. It is computed at each model grid point using monthly temperature and salinity fields and gsw-python package (Firing et al., 2021). The AOU reflects the net effect of biological oxygen consumption and physical ventilation of water masses. It is computed as the residual between modelled O_2 concentrations and their corresponding saturation values.

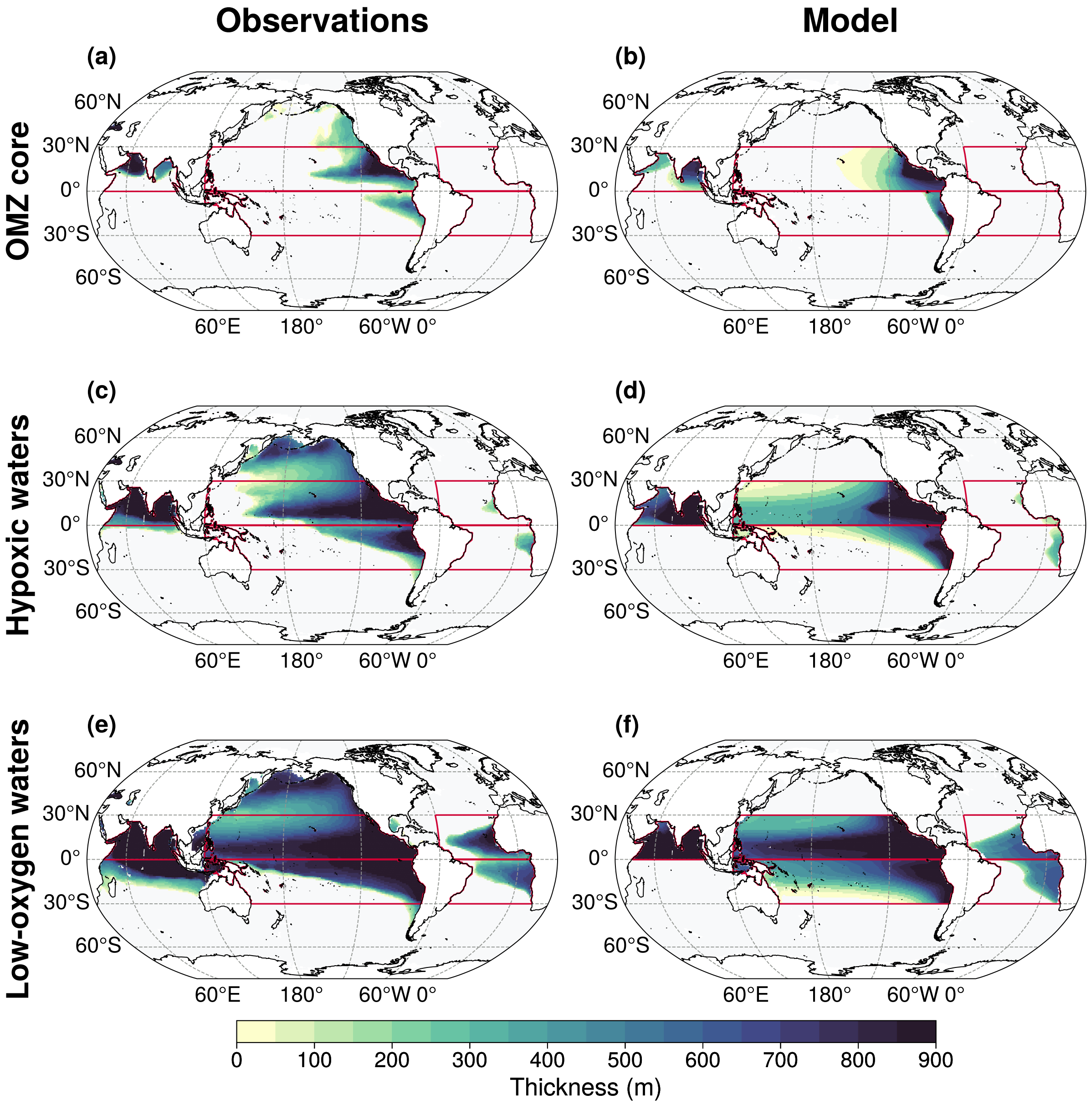

Figure 5. Comparison of $100-1000\mathrm{m}$ OMZ thickness between **(first column)** the World Ocean Atlas climatology and **(second column)** IPSL-CM6A-LR Large Ensemble inter-member mean. The thickness of the **(first row)** OMZ Core, **(second row)** Hypoxic volumes, and **(third row)** Low-oxygen volumes is computed using the volume percentiles defined in Table 1. **Red boxes** indicate the five OMZ regions analysed in the IPSL-CM6A-LR simulations: the tropical North Pacific, tropical South Pacific, tropical North Atlantic, tropical South Atlantic, North Indian

https://doi.org/10.5194/egusphere-2025-2805
Preprint. Discussion started: 23 July 2025

To further interpret AOU variations in the $100 - 1000\mathrm{m}$ depth range, we examine two key drivers: the carbon export flux at $100\mathrm{m}$ and the mean age since surface contact. The carbon export flux serves as a proxy for biological oxygen demand contributing to AOU, while the mean age reflects water masses ventilation.

All variables are extracted or computed prior to the application of the piControl drift correction and are subsequently detrended using the same method applied to the O_2 fields.

2.5 Time of emergence

We use the concept of time of emergence to detect climate-driven changes exceeding internal variability. The time of emergence is defined as the last time step at which the climate-forced signal becomes statistically distinguishable from internal variability, referred to as the noise (Hawkins and Sutton, 2012). This condition is formally expressed as:

$$ToE : \frac{S}{N} \geq 2 \tag{4}$$

where S represents the climate-driven signal and N represents the noise. A ratio of 2 corresponds to a confidence level of 95.45%, ensuring that the detected emergence is robust (Storch and Swiers, 1999).

Each member within the IPSL Large Ensemble contains both the climate-driven signal and the system's internal variability (Deser et al., 2012). By conducting an ensemble of 30 experiments, we are able to separate these two components. The climate signal is estimated by averaging across ensemble members, while internal variability is quantified as the inter-member standard deviation (Deser et al., 2012). For each biogeochemical variables and for previously defined OMZ volumes, climate-driven signals are extracted from anomalies, which are computed relative to the pre-industrial period (1850-1899). Internal variability is time dependant and estimated using absolute values rather than anomalies, which prevents underestimating variability during the pre-industrial reference period. This approach is particularly relevant given that internal variability can evolve under climate change scenarios. It is particularly true in the IPSL-CM6A-LR large ensemble where the spread across ensemble members decreases under future forcing, reflecting the influence of anthropogenic external forcings on internal modes of variability (Bonnet et al., 2021).

Each ensemble member can also be interpreted as a distinct realisation of the climate response to the SSP2-4.5 scenario. Accordingly, we also compute the time of emergence for each individual simulation. In this case, the externally forced signal is taken from a single member, while the internal variability is still estimated using the ensemble standard deviation. This procedure yields a distribution of times of emergence across the ensemble.

3 Results

3.1 Climate-driven OMZ volume signals

Here, we present the ensemble mean climate-driven changes in OMZ Core volumes, Hypoxic volumes and Low-oxygen volumes across each OMZ spatial domain, along their corresponding time-dependent internal variability (Figure 6). We also

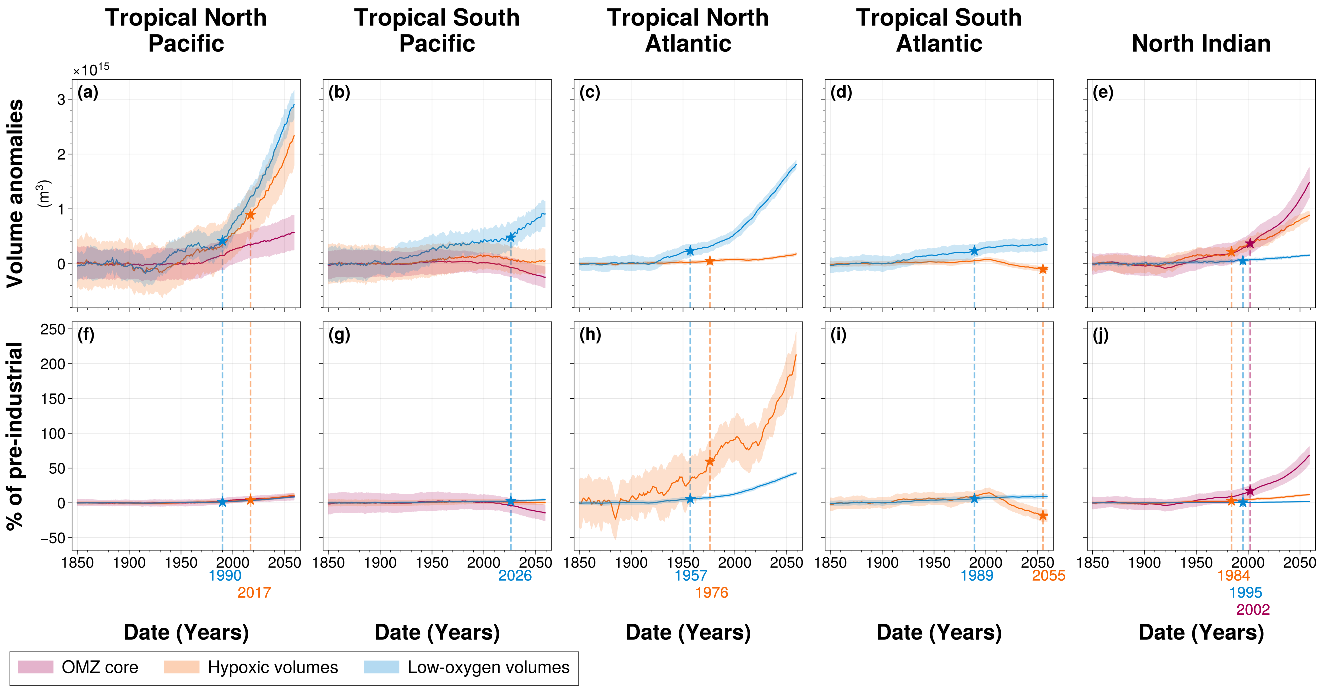

Figure 6. Time of emergence of $100-1000$m OMZ volumes for, from left to right **column**, the tropical North Pacific, the tropical South Pacific, the tropical North Atlantic, the tropical South Atlantic, the North Indian ocean. In all panels, colours represent the $[O_2]$ threshold used to define OMZ volumes : **(purple)** OMZ Core, **(orange)** Hypoxic volumes and **(blue)** low-oxygen volumes. The time of emergence, indicated by the **symbol star** in all panels, occurs when **(solid line)** the ensemble mean exceeds **(coloured area)** the standard deviation over the Large Ensemble. The time of emergence is calculated for the **(first row)** OMZ volume anomalies relative to pre-industrial period (1850-1899) and **(second row)** percentage of pre-industrial mean volume. All times of emergence are indicated on the bottom axis and summarized in the Table 2.

examine the time of emergence of the climate-driven volume signal, defined as the year when the forced signal exceeds twice the magnitude of time-dependent internal variability (Figure 6, Table 2).

3.1.1 Evolution of climate-driven OMZ volume signals

Across all OMZ regions, Low-oxygen volumes exhibit a clear and consistent expansion throughout the simulation (Figure 6). This expansion is particularly pronounced in the tropical North Pacific and tropical North Atlantic, with total volume increases of $2.84 \times 10^{15}\mathrm{m}^3$ and $1.76 \times 10^{15}\mathrm{m}^3$, respectively, by the end of the simulation (Figure 6a, c). However, in all regions except the tropical North Atlantic, this expansion remains below 10% of their pre-industrial mean volumes (Figure 6f–j). Only the tropical North Atlantic Low-oxygen volume shows a strong expansion, reaching 41.8% increase relative to its pre-industrial mean (Figure 6h).

In the South Atlantic, the expansion slows during the SSP2-4.5 period (2015–2059), with a rate of $3.28 \times 10^{12}\mathrm{m}^3.\mathrm{year}^{-1}$

Table 2. Time of emergence of $100-1000\mathrm{m}$ OMZ volume anomalies for the Large Ensemble inter-members mean in each OMZ box. **"No emergence"** indicates that the ensemble mean has not emerged from twice the ensemble standard deviation, across the IPSL Large Ensemble, by the end of the simulation (Figure 6). The symbol **"-"** indicates the absence of OMZ volume in the region of interest.

	Tropical Pacific	Tropical South Pacific	Tropical North Atlantic	Tropical South Atlantic	North Indian
OMZ Cores	No emergence	No emergence	-	-	2002
Hypoxic volumes	2017	No emergence	1976	2055	1984
Low-oxygen volumes	1990	2026	1957	1989	1995

compared to $5.43\times10^{11}\mathrm{m}^3.\mathrm{year}^{-1}$ during the historical period (1970–2014) (Figure 6c, h). In contrast, other OMZ regions exhibit much stronger expansion during SSP2-4.5: the tropical North Pacific shows the fastest growth ($4.19\times10^{13}\mathrm{m}^3.\mathrm{year}^{-1}$), followed by the tropical North Atlantic ($2.29\times10^{13}\mathrm{m}^3.\mathrm{year}^{-1}$), the tropical South Pacific ($1.18\times10^{13}\mathrm{m}^3.\mathrm{year}^{-1}$), and the North Indian Ocean, which has the slowest rate ($1.60\times10^{12}\mathrm{m}^3.\mathrm{year}^{-1}$) (Figure 6a–c, e).

In the tropical North Pacific and tropical North Atlantic, Hypoxic volumes also expand (Figure 6a, c). In the tropical North Pacific, the Hypoxic volume increases by $2.25\times10^{15}\mathrm{m}^3$, corresponding to a 10.6% increase relative to its pre-industrial mean. The tropical North Atlantic only increases by $1.66\times10^{14}\mathrm{m}^3$ but exhibits the largest relative increase of 197% by the end of the simulation as it has the smallest Hypoxic volume among the IPSL Large Ensemble's present-day climatology. These expansions result from increasing rates during the SSP2-4.5 period (2015–2059) of $3.31\times10^{13}\mathrm{m}^3.\mathrm{year}^{-1}$ in the tropical North Pacific and $2.5\times10^{12}\mathrm{m}^3.\mathrm{year}^{-1}$ in the tropical North Atlantic, and corresponding to annual increases of 0.15% and 2.98% of their pre-industrial mean volumes (Figure 6a, c, f, h). Expansion during SSP2-4.5 is substantially stronger than in the present-day period (1970–2014), with growth rates increasing by factors of 2.4 and 3.6, respectively (Figure 6a, c).

In contrast, Hypoxic volumes in the tropical South Pacific and tropical South Atlantic shift from a weak expansion to a contraction trend in 2004 with contraction rates during SSP2-4.5 of -1.66×10^{12} and $-2.89\times10^{12}\mathrm{m}^3.\mathrm{year}^{-1}$, respectively (Figure 6b, d). The contraction in the tropical South Atlantic is particularly marked, exceeding the preceding expansion rate and resulting in a 18% reduction in Hypoxic volume relative to pre-industrial levels. Meanwhile, the tropical South Pacific Hypoxic volume shows no significant net change at the end of the simulation.

OMZ Core volumes show divergent trends between regions. In the tropical North Pacific and tropical North Indian Ocean, they expand slowly in the former ($5.21\times10^{12}\mathrm{m}^3.\mathrm{year}^{-1}$) with a total increase of 9% by the end of the simulation, and more substantially in the latter ($2.09\times10^{13}\mathrm{m}^3.\mathrm{year}^{-1}$) with a total increase of 68% by the end of the simulation (Figure 6a, e, j). Conversely, the OMZ Core in the tropical South Pacific shows a strong contraction resulting in a 14% volume reduction at the end of the simulation which correspond to a contraction rate of $-5.49\times10^{12}\mathrm{m}^3.\mathrm{year}^{-1}$ during the SSP2-4.5 period (Figure 6b, g).

https://doi.org/10.5194/egusphere-2025-2805
Preprint. Discussion started: 23 July 2025

3.1.2 OMZ volume variability

Internal variability of OMZ volumes remains stable throughout the SSP2-4.5 scenario (Figure 6), allowing us to present average variability values over the entire simulation period. In both the tropical North and South Pacific, internal variability of OMZ volumes is higher than in the other regions with maximum variability for the Hypoxic volumes in the tropical North Pacific ($4.38 \times 10^{14}\mathrm{m}^3$) and minimum for the tropical South OMZ Core ($2.08 \times 10^{14}\mathrm{m}^3$) (Figure 6a,b). Thus, in tropical Pacific, internal variability is of comparable magnitude across all OMZ volume classes, despite differences in absolute volume, with OMZ Core volumes being smaller than Hypoxic and Low-oxygen volumes (Figure 6a,b). The tropical Atlantic shows the lowest internal variability, with Hypoxic and Low-oxygen volumes varying by $2.31 \times 10^{13}\mathrm{m}^3$ and $1.16 \times 10^{14}\mathrm{m}^3$, respectively. However, the relative variability of North Atlantic Hypoxic volume is the highest across all regions, reaching 30% of its pre-industrial mean (Figure 6h). In the North Indian Ocean, Hypoxic and OMZ Core volumes exhibit greater mean variability ($1.26 \times 10^{14}\mathrm{m}^3$ and $1.89 \times 10^{14}\mathrm{m}^3$, respectively) compared to Low-oxygen volumes ($2.72 \times 10^{13}\mathrm{m}^3$).

3.1.3 Time of emergence of climate-driven OMZ volume signals

With the exception of the North Indian Ocean, the climate-driven signal in Low-oxygen volumes emerges from internal variability earlier than in the other types of OMZ volumes, making it the earliest detectable signal of change in all OMZ regions. Emergence of this signal occurs as early as 1957 in the tropical North Atlantic, followed by 1989 in the tropical South Atlantic, 1990 in the tropical North Pacific, and 2026 in the tropical South Pacific (Figure 6a–d, Table 2). These timings reveal a hemispheric asymmetry: the signal emerges 36 years earlier in the tropical North Pacific than in the tropical South Pacific, and 32 years earlier in the tropical North Atlantic than in the tropical South Atlantic (Figure 6a–c, Table 2). However, emergence in the tropical North Atlantic leads that of the tropical North Pacific by 33 years (Figure 6a, c, Table 2).
In the North Indian Ocean, however, although all three volume categories show detectable climate-driven signals emergence before the end of the simulation, the Low-oxygen volume climate-driven signal emerges in 1995 (Figure 6e).

In both the tropical Pacific and tropical Atlantic, the climate-driven signal expansion in Hypoxic volumes either emerges later than in Low-oxygen volumes or does not emerge at all within the 210-year simulation period. In the tropical North Atlantic and tropical North Pacific, emergence occurs in 1976 and 2017, respectively (Figure 6a, c, Table 2). In the tropical South Atlantic, although the signal initially follows a slow expansion, a sharp reversal leads to contraction, with emergence detected in 2055 (Figure 6a, c, Table 2). In contrast, the Hypoxic volume signal in the tropical South Pacific does not emerge before the end of the simulation with no significant changes compared to pre-industrial era (Figure 6a, c, Table 2). In the North Indian Ocean, Hypoxic volume expand and the climate-driven signal emerge from internal variability in 1984 (Figure 6e, Table 2).

In both the tropical North and South Pacific, although the OMZ Core volumes expand and contract, respectively, the climate signal does not exceed twice the range of internal variability, and therefore does not emerge within the simulation period. In the North Indian Ocean, the OMZ Core forced signal emerge in 2002 (Figure 6e, Table 2).

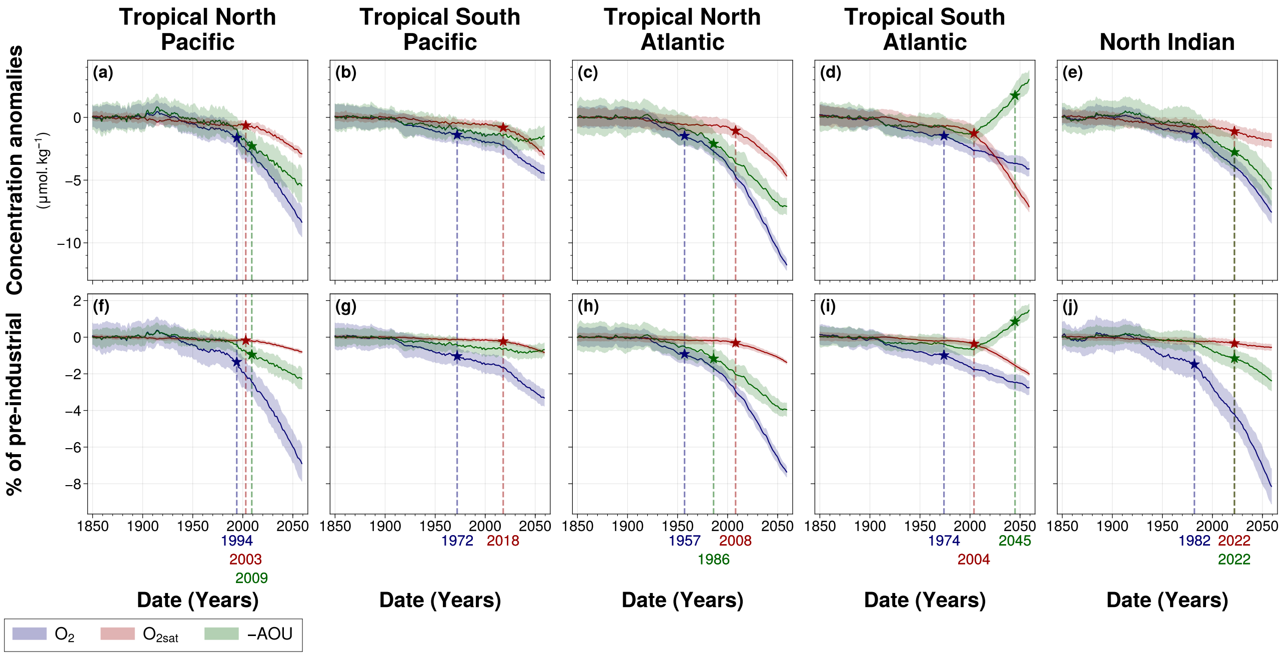

Figure 7. Time of emergence of $100-1000\mathrm{m}$ spatial mean concentrations of **(blue)** O_2, **(red)** O_{2sat} and **(green)** $-AOU$ in the IPSL Large Ensemble for **(columns)** each OMZ box. The time of emergence (indicated by the **star symbol**) is defined as the point at which **(first row)** the mean concentration anomalies, and **(second row)** the percentage of pre-industrial concentrations, averaged across the Large Ensemble, exceed their respective **(coloured areas)** standard deviations within the Large Ensemble.

3.2 Deoxygenation and its drivers in each OMZ spatial domains

Here, we present climate-driven changes in mean dissolved oxygen concentration and its associated drivers ($O_{2,sat}$ and AOU) across each OMZ spatial domain, along with their corresponding time-dependent internal variability (Figure 7). We also examine the time of emergence of these climate-driven signals, defined as the year when the forced signal exceeds twice the magnitude of time-dependant internal variability (Figure 7, Table 3).

All OMZ regions exhibit a decline in mean dissolved oxygen concentrations throughout the simulation (Figure 7). The northern parts of the tropical Pacific and tropical Atlantic OMZs show the most pronounced deoxygenation, with decreases in dossolved oxygen concentration of $-8.12\mathrm{\mu mol.kg^{-1}}$ and $-11.5\mathrm{\mu mol.kg^{-1}}$, respectively, by the end of the simulation (Figure 7a, c). These losses are stronger than those observed in their southern counterparts, which decline by $-4.40\mathrm{\mu mol.kg^{-1}}$ and $-4.04\mathrm{\mu mol.kg^{-1}}$, respectively (Figure 7b, d). With the exception of the tropical South Atlantic, all regions experience an acceleration in deoxygenation during the SSP2-4.5 period (2014–2059) compared to the present-day period (1970–2014) (Figure 7). In the tropical South Atlantic, however, deoxygenation follows a nearly linear trend, with a present-day rate of $-3.48\times10^{-2}\mathrm{\mu mol.kg^{-1}.year^{-1}}$ and a slightly slower rate of $-2.86\times10^{-2}\mathrm{\mu mol.kg^{-1}.year^{-1}}$ during SSP2-4.5. During the SSP2-4.5 period, oxygen loss is more severe in the Northern Hemisphere OMZ regions: the tropical North Pacific experiences

https://doi.org/10.5194/egusphere-2025-2805
Preprint. Discussion started: 23 July 2025

Table 3. Time of emergence of $100-1000\text{m}$ spatial mean concentration anomalies for the Large Ensemble inter-members mean in each OMZ box. **"No emergence"** indicates that the ensemble mean has not emerged from twice the ensemble standard deviation, across the IPSL Large Ensemble, by the end of the simulation (Figure 7).

	Tropical Pacific	Tropical South Pacific	Tropical North Atlantic	Tropical South Atlantic	North Indian
O_2	1994	1972	1957	1974	1982
O_{2sat}	2003	2018	2008	2004	2022
$-AOU$	2009	No emergence	2986	2045	2022

deoxygenation at twice the rate of the tropical South Pacific, and the tropical North Atlantic at more than five times the rate of its southern counterpart (Figure 7f–i). The North Indian Ocean undergoes the most significant oxygen decline of all regions, with an 8.1% reduction relative to its pre-industrial mean by the end of the simulation (Figure 7j).

In all regions, the climate-driven deoxygenation signal emerges from internal variability before the end of the simulation period (Figure 7, Table 3) These signals emerge after the mid-20th century in all regions and before 21st century, beginning in the tropical North Atlantic in 1957, followed by the tropical South Pacific and South Atlantic in 1972 and 1974, respectively, then the North Indian Ocean in 1982, and finally the tropical North Pacific in 1994 (Figure 7, Table 3).

Decomposition of the oxygen signal into contributions from oxygen solubility (O_{2sat}) and apparent oxygen utilisation ($-AOU$) reveals contrasting dynamics. A decrease in O_{2sat} emerges in all regions during the first quarter of the 21st century, while the $-AOU$ signal shows regionally divergent trends: it declines and exceeds their internal variability in the North Pacific, North Atlantic, and North Indian Ocean, but increases in the tropical South Pacific and the tropical South Pacific (Figure 7, Table 3).

In all regions, the O_{2sat} decrease signal emerges after the deoxygenation signal (Figure 7, Table 3). These signal decline gradually until 2000, after which it accelerates sharply and continues to decrease throughout the simulation period (Figure 7a–e). In all regions, the decline rate increases by a factor 10 between the present-day and SSP2-4.5 periods (Figure 7a–e). Emergence occurs close to or shortly after this inflection point: in 2003 in the North Pacific, 2004 in the South Atlantic, 2008 in the North Atlantic, 2018 in the South Pacific, and 2022 in the North Indian Ocean (Figure 7, Table 3). The acceleration is accompanied by a reduction in signal variability, consistent with emergence occurring near the inflection point (Figure 7).

Although all OMZ regions display a consistent trend of deoxygenation and O_{2sat} decline, the $-AOU$ component shows contrasting behaviours between hemispheres. In the tropical North Pacific and tropical North Atlantic, $-AOU$ decreases by -5.34µmol.kg^{-1} and -7.08µmol.kg^{-1}, respectively, by the end of the simulation (Figure 7a, c). The emergence of this signal occurs later in the tropical North Pacific (2009) than in the tropical North Atlantic (1986) (Figure 7a, c; Table 3). In contrast, the tropical South Atlantic initially exhibits a slow decrease in $-AOU$ at a rate of $-4.95\times10^{-3}\text{µmol.kg}^{-1}.\text{year}^{-1}$, followed by a sharp increase after 2004 at a rate of $8.59\times10^{-2}\text{µmol.kg}^{-1}.\text{year}^{-1}$. This reversal results in a total increase

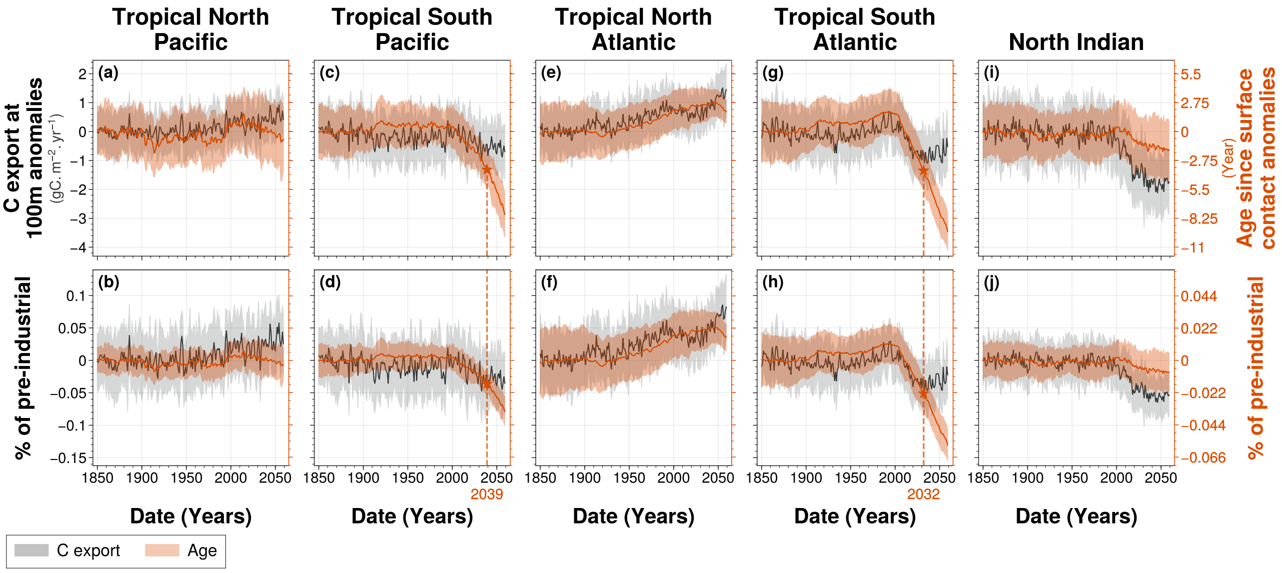

Figure 8. Spatial mean across **(columns)** each OMZ spatial box of **(grey)** carbon export anomalies at 100m depth and **(orange)** age since surface contact anomalies between 100 and 1000m depth. **Solid lines** represent **(first row)** the inter-members mean anomalies relative to pre-industrial period (1850-1900) and **(second row)** the percentage of pre-industrial mean, while the **shaded areas** correspond to their respective inter-members standard deviation within the IPSL Large Ensemble. **Star symbols** indicate the time of emergence, defined as the point at which **(solid lines)** the ensemble mean exceeds **(coloured areas)** the standard deviation within the Large Ensemble.

of $2.79\mu\mathrm{mol.kg}^{-1}$ by the end of the simulation. The positive $-AOU$ anomalies in this region become distinguishable from internal variability in 2045 (Figure 7b, d; Table 3). In the tropical South Pacific, the $-AOU$ signal does not show a distinct inflection point but shows a slower decreasing trend during SSP2-4.5 period, with a rate of $-6.66\times10^{-3}\mu\mathrm{mol.kg}^{-1}.\mathrm{year}^{-1}$, compared to $-1.13\times10^{-2}\mu\mathrm{mol.kg}^{-1}.\mathrm{year}^{-1}$ during the present-day period. In the North Indian Ocean, $-AOU$ follows a decreasing trajectory, with its signal emerging concurrently with that of O_{2sat} in 2022 (Figure 7e; Table 3).

3.3 Biological and ventilation dynamics

Here, we present the ensemble-mean, climate-driven changes in mean carbon export at 100m and mean age since surface contact across each OMZ spatial domain, along with their corresponding time-dependent internal variability (Figure 8). We also examine the time of emergence of these climate-driven signals, defined as the year when the forced signal exceeds twice the magnitude of internal variability (Figure 8).

By disentangling the effects of biological activity and ventilation, the abrupt shift in the $-AOU$ signal at the year 2004 in the tropical North Atlantic coincides with simultaneous changes in both carbon export and water mass age (Figure 8).

Before 2004, carbon export remains stable across all OMZ regions, except in the tropical North Atlantic, where it increases at an annual increase of $9.35\times10^{-3}\mathrm{gC.m}^{-2}.\mathrm{year}^{-1}$ (Figure 8a–e). The North Indian Ocean shows the highest mean carbon

https://doi.org/10.5194/egusphere-2025-2805
Preprint. Discussion started: 23 July 2025

export before 2004, with an export rate of 32.57×10^{-1}gC.m^{-2}.year^{-1}. In contrast, tropical Pacific and tropical Atlantic OMZ regions exhibit a hemispheric asymmetry. The Southern Hemisphere presents higher carbon export rates of 19.31×10^{-1}gC.m^{-2}.year^{-1} in the tropical South Pacific and 23.48×10^{-1}gC.m^{-2}.year^{-1} in the tropical South Atlantic compared to their Northern Hemisphere counterparts, which have an export of 16.28×10^{-1} and 17.80×10^{-1}gC.m^{-2}.year^{-1}, respectively. After 2004, a pronounced decline in carbon export is observed over approximately two decades in the North Indian Ocean, tropical South Atlantic, and tropical South Pacific, before stabilising toward the end of the simulation (Figure 8b, d, e). The cumulative decline in carbon export over this period reaches -1.69gC.m^{-2}.year^{-1} in the North Indian Ocean, -6.25×10^{-1}gC.m^{-2}.year^{-1} in the tropical South Atlantic, and -6.98×10^{-1}gC.m^{-2}.year^{-1} in the tropical South Pacific. In contrast, the tropical North Atlantic exhibits stable carbon export during this period, followed by a continued gradual increase at a rate similar to that observed before 2004 (Figure 8d). Meanwhile, the tropical North Pacific shows a steady post-2004 increase in carbon export, at an annual increase of 4.61×10^{-3}gC.m^{-2}.year^{-1} (Figure 8c).

Before 2004, the age since surface contact shows no significant variations in any OMZ regions, except in the tropical North Atlantic, where it begins increasing in 1925 at a steady rate of 3.78×10^{-2}year.year^{-1}, continuing through the end of the simulation (Figure 8a). The tropical Pacific exhibits the highest mean age since surface contact before 2004, with values of 263years in the tropical North Pacific and 227years in the tropical South Pacific. In contrast, the tropical Atlantic shows lower values, with 122years in the tropical North Atlantic and 166years in the tropical South Atlantic. After 2004, the age since surface contact decreases sharply in the tropical Southern Hemisphere OMZ regions, with total reductions of -7.30years in the tropical South Pacific and -8.96years in the tropical South Atlantic by the end of the simulation. These represent declines of -3.21% and -5.43% relative to their respective pre-industrial means. The corresponding rates of decline are -2.04×10^{-1}year.year^{-1} in the tropical South Atlantic and -1.51×10^{-1}year.year^{-1} in the tropical South Pacific (Figure 8b, d). A slower decline is also observed in the North Indian Ocean, with a rate of -2.77×10^{-2}year.year^{-1} (Figure 8e). These changes lead to the emergence of the ventilation signal from internal variability in 2032 in the tropical South Atlantic and in 2039 in the tropical South Pacific. In the tropical North Pacific, the age since surface contact also begins to decline around 2004, although at a slower rate of -3.99×10^{-2}year.year^{-1} (Figure 8c).

3.4 Time of Emergence distribution within the IPSL-CM6A-LR Large Ensemble

Here, we present the ensemble distribution of the time of emergence of climate-driven changes in mean dissolved oxygen concentration and OMZ volumes across each OMZ spatial domain (Figure 9). We show the corresponding boxplots, along with the time of emergence and associated trend sign for each ensemble member (Figure 9).

For OMZ volumes and dissolved oxygen concentrations, the sign of the trend at the time of emergence of the ensemble mean is further supported by the emergence of individual ensemble members (Figure 9). In cases where the Large Ensemble mean does not emerge by the end of the simulation, some individual members nonetheless show emergence. They are members with either stronger forced trends or lower internal variability, and thereby corroborate the trend direction of the ensemble mean. This is particularly evident in the tropical South Pacific and tropical South Atlantic, where individual members exhibit clear emergence of OMZ Core and Hypoxic volume contraction (Figure 9b, d).

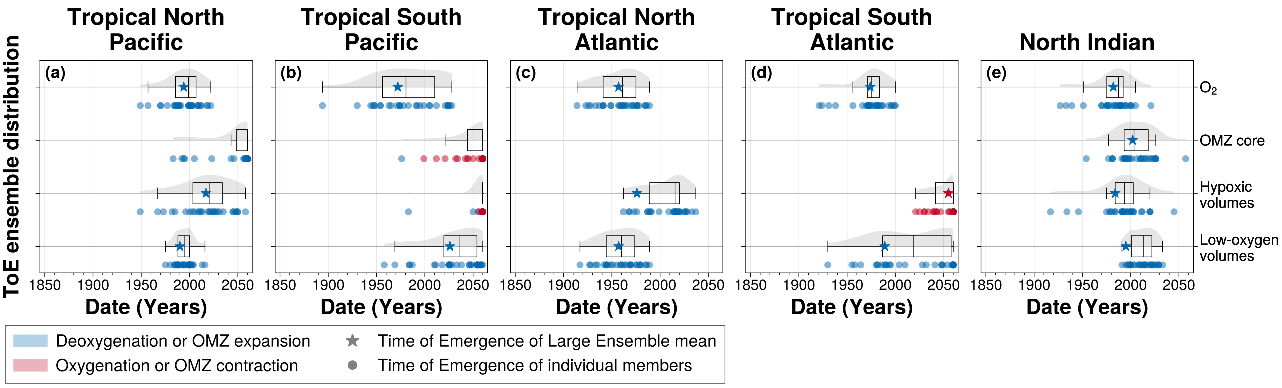

Figure 9. Distribution of the time of emergence within the IPSL Large Ensemble for **(columns)** each OMZ box. Time of emergence is computed for $100-1000\mathrm{m}$ **(first row)** spatial mean concentration anomalies of O_2 and OMZ volume anomalies for **(second row)** OMZ Core, **(third row)** Hypoxic volumes and **(fourth row)** Low-oxygen volumes. In all panels, the **box plots** illustrate the dispersion of the time of emergence around the median across the IPSL Large Ensemble, while the **violin plots** illustrate the distribution of the time of emergence within the IPSL Large Ensemble. The **star symbol** represents the time of emergence for the Large Ensemble mean when it exceeds the Large Ensemble standard deviation, while the **dots** represent the time of emergence for individual ensemble members signal when they exceed the piControl standard deviation. Their colours indicate the sign of their trend at the emergence: **blue** for deoxygenation or OMZ expansion, and **red** for oxygenation or OMZ contraction.

Across all OMZ regions, the ensemble mean generally underestimates the time of emergence compared to the ensemble median, with large spread quantified by the interquartile range (Figure 9). The North Indian Ocean stands out as the only region where all metrics (dissolved oxygen concentrations and OMZ volumes) exhibit a narrow emergence window, with spreads limited to 17 years for oxygen signal and 25 years for OMZ Core volumes (Figure 9e). In contrast, broader spreads in other regions are linked either to weaker trend magnitudes at the time of emergence, as in the tropical South Pacific where deoxygenation shows an interquartile range of 54 years, or to trend inflections that change the trend sign, such as in the tropical South Atlantic where the low-oxygen volume signal displays a 71-year spread (Figure 9b, d).

In all regions except the North Indian Ocean, the ensemble mean for dissolved oxygen concentration emerges earlier than, or concurrently with, the Low-oxygen volume ensemble mean (Figure 9). However, due to the large inter-member spread in time of emergence, the distributions of deoxygenation and OMZ volumes time of emergence overlap in all regions (Figure 9).

4 Discussion

4.1 Emerging low oxygen volume expansion in OMZ

Among the three OMZ regimes, only the Low-oxygen volume exhibits a consistent expansion with a detectable emergence of the climate-driven signal from internal variability across all OMZ regions (Figure 6). This result is consistent with the

https://doi.org/10.5194/egusphere-2025-2805
Preprint. Discussion started: 23 July 2025

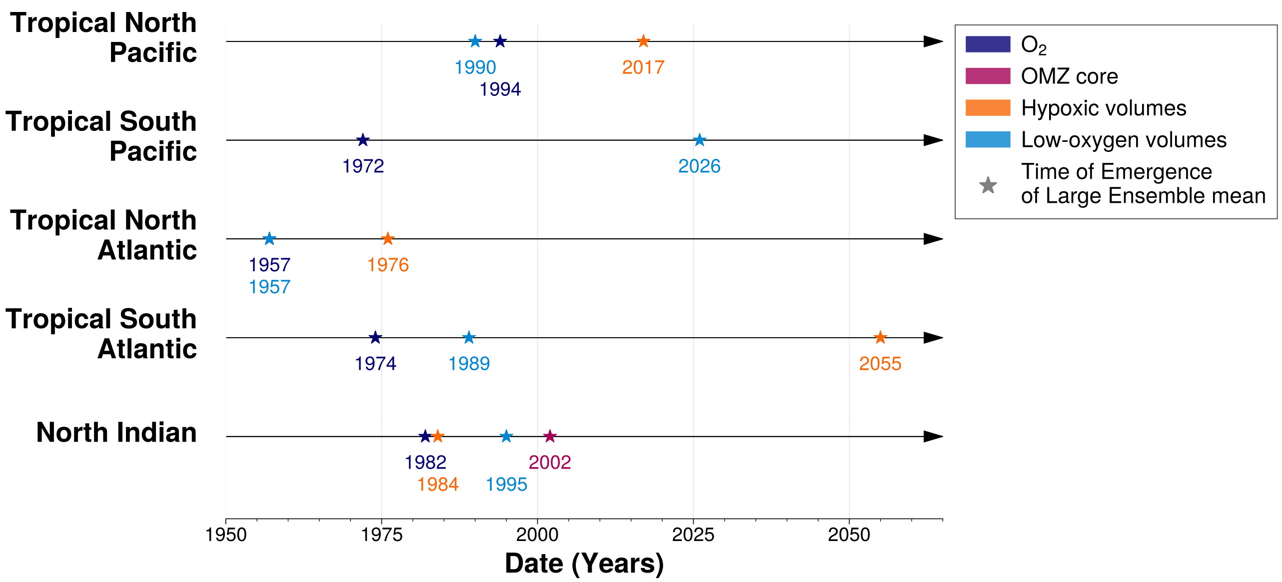

Figure 10. Time of Emergence of Large Ensemble mean for **(rows)** each OMZ box. The time of emergence, represented by the **star symbol**, is computed for $100-1000$m **(dark blue)** spatial mean concentration anomalies of O_2 and OMZ volume anomalies for **(purple)** OMZ Core, **(orange)** Hypoxic volumes and **(light blue)** Low-oxygen volumes.

findings of Ditkovsky et al. (2023), who showed that OMZ volumes defined using higher oxygen thresholds expand across all OMZ regions. A comparison of their time of emergence also reveals regional offsets between ocean basins. Specifically, the tropical Atlantic OMZ shows an earlier emergence, by approximately two to three decades, compared to the tropical Pacific OMZ (Figure 10). This earlier emergence is not due to faster expansion, but rather to lower internal variability of the tropical Atlantic Low-oxygen volumes, which makes the climate-driven trend detectable before the tropical Pacific Low-oxygen volumes expansion (Figure 6).

Although Low-oxygen volumes expand in all OMZ regions, subdividing the tropical Pacific and tropical Atlantic OMZs into northern and southern subregions reveals a consistent 30-year delay in the emergence of Low-oxygen volumes in the Southern Hemisphere compared to the Northern Hemisphere (Figure 10). While internal variability remains similar across hemispheres within each basin, the magnitude of the climate-driven trend is stronger in the Northern Hemisphere in both basins (Figure 6). A similar hemispheric asymmetry is observed in the mean deoxygenation trends, where Northern Hemisphere regions exhibit stronger climate-driven declines in oxygen concentrations compared to their Southern counterparts (Figure 7).

Low-oxygen volumes are critical as they influence the distribution of habitable zones for many marine species (Bertrand et al., 2011). In the IPSL-CM6A-LR model, the emergence of tropical Atlantic Low-oxygen volumes occurs earliest, impacting oxygen-dependant ecosystem sooner than in other OMZ regions. Moreover, Northern Hemisphere ecosystems may face earlier and more intense disruptions from expanding low-oxygen volumes, while Southern Hemisphere systems may experience more gradual but persistent changes.

4.2 Inter-hemispheric contrast in emerging OMZ Core and Hypoxic volume change

The north-south subdivision of the OMZs shows asymmetric dynamics between the North and South parts of the OMZs. The Core of the OMZs only expands in the northern hemisphere by the end of the simulation while they are shrinking in their southern counterpart (Figure 6). The tropical South Pacific and tropical South Atlantic OMZs show a contraction of their volume with lowest oxygen concentration, the OMZ Core in the former and Hypoxic waters in the latter, which is consistent with the findings of Busecke et al. (2022); Ditkovsky et al. (2023) (Figure 6). In both tropical Pacific and tropical Atlantic, the southern OMZ Core is being ventilated by younger water masses (Figures 7, 8). This is consistent with the single-pipe and mixing network ventilation framework developed by Gnanadesikan et al. (2007, 2012). It suggests that in a warmer and more stratified ocean, such as the future ocean, the proportion of different ventilation sources shifts, favouring younger subsurface waters. In the tropical South Atlantic, ventilation is provided by through younger subsurface waters originating from the South Indian Ocean, which are advected into the South Atlantic via the Agulhas Current. In the tropical South Pacific, ventilation occurs through water masses from the southern Pacific basin, which are advected northward by the Humboldt Current. This ventilation process is co-located with southern OMZ Core location in the geographic-space (Figures 8, A1). This oxygenation trend in the tropical South Atlantic basin is also show by CMIP6 multi-model mean over the present-day period in (Takano et al., 2023) and by the end of the 21st century over SSP1-2.6 and SSP5-8.5 showed in (Kwiatkowski et al., 2020).

Unlike previous findings by Ditkovsky et al. (2023), our results do not show a contraction of the OMZ Core in the North Indian. This discrepancy likely stems from misrepresentation of oxygen concentrations and deoxygenation patterns in the IPSL-CM6A-LR model. The Large Ensemble simulations of the IPSL misrepresent oxygen levels in the North Indian, failing to capture the low-oxygen conditions observed in the Arabian Sea (Figure 2). This bias is partly attributable to an overestimation of oxygen concentrations in marginal seas (the Persian Gulf and the Red Sea), combined with poorly constrained outflow parametrisations and a ventilation of the Arabian Sea OMZ by Southern Ocean water masses, where oxygen levels are overestimated (Schmidt et al., 2021). Furthermore, the model fails to reproduce the specific spatial patterns of oxygenation and deoxygenation identified in Ditkovsky et al. (2023) (Figure 3). Specifically, Ditkovsky et al. (2023) describes a distinct dipole structure with an oxygenation pool between 10°N and 10°S along the western boundary, and a deoxygenation pool between 10°S and 30°S along the eastern boundary. This dipole structure supports a double-pipe ventilation mechanism within the North Indian basin. In contrast, the IPSL-CM6A-LR model simulates a broad deoxygenation trend across the basin and fails to capture this ventilation pattern (Figure 3).

4.3 Time of emergence of regional deoxygenation relative to OMZ volumes

In the IPSL Large Ensemble, the mean deoxygenation signal emerges from natural variability across all OMZ regions before the end of the 20th century (Figure 10). With the exception of the North Pacific, this climate-driven deoxygenation signal appears earlier than the expansion signals of OMZ volumes (Figure 10). In both the tropical North Pacific and tropical North Atlantic, the emergence of deoxygenation coincides with the expansion of Low-oxygen volumes, where both deoxygenation and Low-oxygen volume expansion are greater than in their respective Southern Hemisphere (Figures 6, 7, and 10). The mean deoxygenation signal in these regions serves as an indicator of the expansion of OMZ boundaries, which affects the distribution of marine ecosystems. In Southern part of the two OMZ regions, deoxygenation emerges before the Low-oxygen volumes and the others OMZ volumes. Hypoxic waters, which are harmful or lethal to many marine organisms, emerge after the mean deoxygenation signal, with a delay of 27 years in the North Pacific and 19 years in the North Atlantic (Figure 10).

Previous study of Hameau et al. (2020) assessed multi-model time of emergence analysis of the deoxygenation at each grid cell point and at global scale for the Couple Model Intercomparaison Project Phase 5 models (CMIP5, Taylor et al. (2012)) under RCP8.5 scenario (Moss et al., 2010). Hameau et al. (2020) showed a mean of the oxygen time of emergence in the first part of the 21st century at a global scale, with an mean emergence in the CMIP5 IPSL-CM5A-LR in 2019. At local scale they show time of emergence in the second part of the 21st century. These results are consistent with local emergence in the IPSL-CM6A-LR Large Ensemble mean (Figure A1, Table A1). In all OMZ regions, the spatial median of the emergence at each grid cell emerge after the average dissolved oxygen trend across the region (Figure A1, Table A1). Except for the tropical North Atlantic where the median is in 1983, the spatial medians of the emergences are in the first part of the 21st century (Table A1). The median of the oxygen emergence at each grid cell represents the emergence of climate-driven changes, either oxygenation or deoxygenation trend. However, as the evolution of the OMZ volumes are the sum of all oxygen changes in their respective regions, the emergence of mean dissolved oxygen in the OMZ regions better represents the evolution of Low-oxygen waters in the IPSL simulations.

The dispersion of the spatial distribution, within the OMZ regions, of time of emergence is significant (Figure A1, Table A1). This dispersion is consistent with the study of Long et al. (2016) which assesses oxygen time of emergence in the Community Earth System Model large ensemble (CESM Large Ensemble, Kay et al. (2015)) under RCP8.5 scenario. The spread of time of emergence within the OMZ regions reflects the delay of emergence between the three OMZ volumes of interest.

4.4 Sensitivity of the time of emergence of OMZ volumes to the reference period

In this study, we determine the emergence of OMZ volumes relative to pre-industrial using the IPSL-CM6A-LR model. Model simulations provide access to a pre-industrial baseline that is not available in current observational records, making it possible to characterise the full magnitude of climate-driven changes. However, observational oxygen datasets, such as the IAP dataset (Cheng and Gouretski, 2023), only cover the period from 1960 to the present and contain limited data within OMZs. As a result, using these datasets would only allow us to determine the emergence of deoxygenation and reconstructed OMZ volumes relative to the 1960–1970 period. The IPSL Large Ensemble simulations allow us to adopt the 1960–1970 period as a reference to compute time of emergence, providing an estimate of when climate-driven signals in OMZ volumes may become detectable using observation datasets. Using the same method as our previous analysis, times of emergence of dissolved oxygen and OMZ volumes anomalies are computed relative to the 1960–1970 period for both the ensemble mean and individual members. Internal variability is estimated by the inter-member standard deviation.

Except for the Hypoxic volume in the South Atlantic, all time of emergence distributions shift towards later emergence times, with the ensemble-mean emergence delayed by up to 59 years (Figure A2). However, all ensemble-mean signals that emerged with a pre-industrial reference also emerge before the end of the simulation (2059) when the 1960–1970 reference is used

(Figure A2). Thus the climate-driven emergence of OMZ volumes is ongoing, although it remains challenging to detect in observations. The detection challenge arises from the difficulty of measuring OMZ volumes and accurately estimating their natural variability, which is entangled with their anthropogenic response.

4.5 Limitations

The IPSL-CM6A-LR model exhibits a positive bias in dissolved oxygen concentrations, particularly in the OMZs regions. This bias challenges the use of the classical definition of OMZ volumes in model outputs using fixed oxygen concentration thresholds. To address this issue, we adopt the oxygen-ventilation framework developed by Ditkovsky and Resplandy (2025), and define OMZ volumes using fixed volume-percentile thresholds in oxygen-ventilation space. To evaluate the sensitivity of our results to the chosen OMZ volume definition, we compare time of emergence estimates for OMZ volumes based on both the fixed-threshold and fixed volume-percentile approaches (Figure A3). In both cases, time of emergence is computed using pre-industrial anomalies, and internal variability is estimated from the inter-member standard deviation of OMZ volumes.

The percentile-based approach enables the detection of OMZ Core emergence in regions where the fixed-threshold method fails to capture OMZ Core volume. In the tropical Pacific, the classical definition does not capture the reduction of OMZ Core volume in the southern subregion, which becomes apparent when using the percentile-based framework (Figure A3a–b). This approach also reveals an expansion of the OMZ Core in the northern tropical Pacific (Figure A3a). For Hypoxic volumes, both definitions yield consistent trends across regions, with similar signs of climate-driven change: expansions in the northern tropical Pacific, northern tropical Atlantic, and northern Indian Ocean, and contractions in the southern tropical Pacific and Atlantic (Figure A3f–j). However, the percentile-based approach shows emergence of the ensemble mean trends, particularly in the northern tropical basins, where the fixed-threshold method fails to detect emergence. This indicates that, the percentile-based approach allows for the emergence of Hypoxic volume dynamics to be robustly identified in the model output, where the classical approach underestimates or misses these signals due to biased baseline oxygen levels. In contrast, the time of emergence of low-oxygen volumes is relatively insensitive to the method used to define OMZs (Figure A3k-o). This reflects the smaller oxygen bias at higher concentrations in IPSL-CM6A-LR, making the spatial extent of these volumes more robust across definitions and ocean basins (Figure A3k–o). Finally, in the North Indian Ocean, where the model's ventilation bias dominates, the definition method has a negligible effect on time of emergence distributions.

The time of emergence is highly sensitive to the representation and the measures of the internal variability of the signal of interest (Hameau et al., 2019). In our study, internal variability of the signal was measured by the inter-members spread within the IPSL-CM6A-LR Large Ensemble. The 2000 years piControl simulation also provides a representation of the internal variability of the system. It provides an estimate of internal variability taking into account the decadal and millennial internal variability, but as this simulation was run under pre-industrial conditions, it does not account for the effects of historical and SSP2-4.5 forcing on internal variability. To quantify its variability, we compute the standard deviation of the signal over the 2000 years of piControl simulation. Using this constant estimate of internal variability, we compute the time of emergence for the ensemble mean and each of the members.

The emergence of the ensemble mean signal is not significantly affected by the choice of internal variability (Figure A4). However, with internal variability from piControl, the emergence distribution within the IPSL Large Ensemble is stretched towards later times of emergence which is consistent with the results of Hameau et al. (2019) (Figure A4). Using the model CESM1 with scenario RCP8.5, Hameau et al. (2019) exhibit a lower variability using the standard deviation of the residual variability (difference between the annual model output and a low-pass filtered signal) rather than control simulation standard deviation. Thus, time of emergence occurs later taking when using internal variability of piControl simulation. Internal variability of piControl simulation remains a reasonable approximation of simulated natural variability for time of emergence analysis.

5 Conclusions

We used the IPSL-CM6A-LR Large Ensemble to explore how climate-driven deoxygenation affects OMZ. We find that the mean deoxygenation trend primarily reflects the expansion of OMZ Low-oxygen waters. This expansion emerges as a climate-driven signal at the same time as the mean deoxygenation trend in OMZ areas. In contrast, OMZ Cores do not expand. Instead, they contract, delaying their emergence. This contraction is particularly evident in the Southern Hemisphere, where extra-tropical ventilation pathways play a key role in maintaining oxygen levels. As a result, OMZ Core volumes do not emerge from internal variability before the end of the simulation. Overall, our findings suggest that climate-driven deoxygenation is already reshaping OMZ volumes and climate-driven expansions of OMZ volumes are already emerging from natural variability, with significant consequences for marine ecosystems.

https://doi.org/10.5194/egusphere-2025-2805
Preprint. Discussion started: 23 July 2025

Appendix A: Supplementary materials

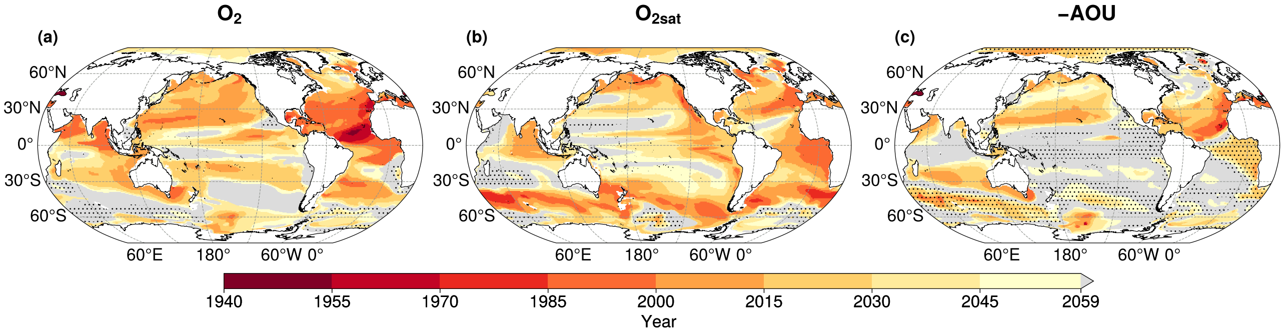

Figure A1. Time of emergence in IPSL-CM6A-LR for the $100-1000\mathrm{m}$ mean concentration of **(a)** dissolved oxygen, **(b)** oxygen saturation and **(c)** the opposite of the apparent oxygen utilisation. **Grey regions** indicate area where no emergence of the anthropogenic signal occurs by the end of the simulation in 2059. **Dashed areas** represent regions where **(a)** O_2, **(b)** O_{2sat} and **(c)** $-AOU$ decrease under the SSP2-4.5 scenario (2014-2059).

Table A1. Average time of emergence of $100-1000\mathrm{m}$ spatial mean concentration anomalies for the Large Ensemble inter-members mean in each OMZ box. Uncertainty is define as the spatial standard deviation of time of emergence across each OMZ spatial box.

	Tropical North Pacific	Tropical South Pacific	Tropical North Atlantic	Tropical South Atlantic	North Indian
O_2	2028 ± 18	2040 ± 16	1984 ± 13	2020 ± 24	2008 ± 17
O_{2sat}	2039 ± 19	2040 ± 18	2019 ± 20	2008 ± 14	2034 ± 22
$-AOU$	2049 ± 18	2058 ± 7	2023 ± 22	2038 ± 17	2047 ± 18

https://doi.org/10.5194/egusphere-2025-2805
Preprint. Discussion started: 23 July 2025

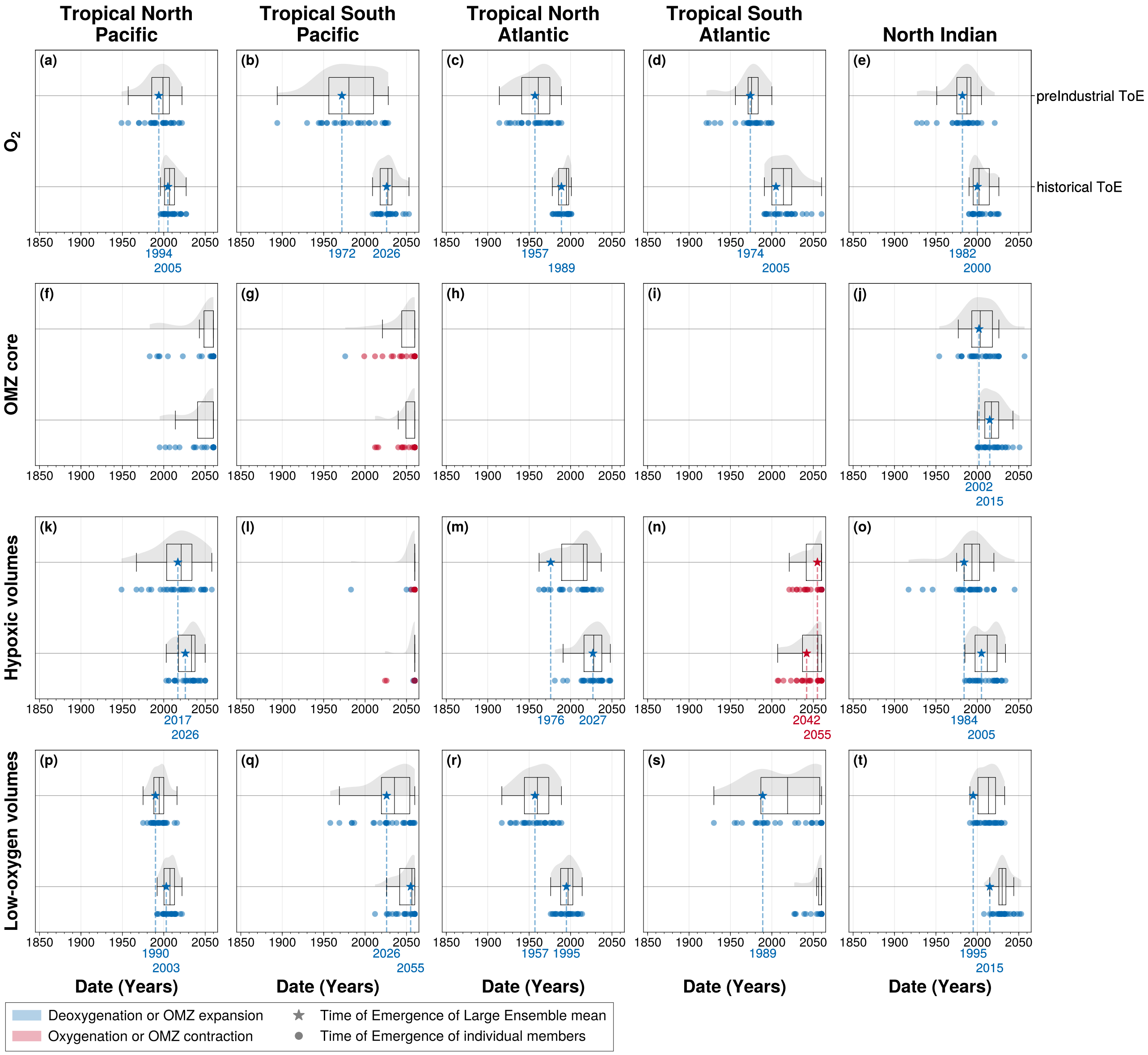

Figure A2. Time of emergence of **(panels' first line)** pre-industrial (1850-1900) versus **(panels' second line)** historical (1960-1970) anomalies in **(columns)** each OMZ box. Times of emergence are computed for $100-1000$m **(first row)** spatial mean concentration anomalies of O_2 and OMZ volume anomalies for **(second row)** OMZ Core, **(third row)** Hypoxic volumes and **(fourth row)** Low-oxygen volumes. In all panels, the **box plots** illustrate the dispersion of the time of emergence around the median across the IPSL Large Ensemble, while the **violin plots** illustrate the distribution of the time of emergence within the IPSL Large Ensemble. The **star symbol** represents the time of emergence for the Large Ensemble mean when it exceeds the Large Ensemble standard deviation, while the **dots** represent the time of emergence for individual ensemble members signal when they exceed the piControl standard deviation. Their colours indicate the sign of their trend at the emergence: **blue** for deoxygenation or OMZ expansion, and **red** for oxygenation or OMZ contraction.

https://doi.org/10.5194/egusphere-2025-2805
Preprint. Discussion started: 23 July 2025

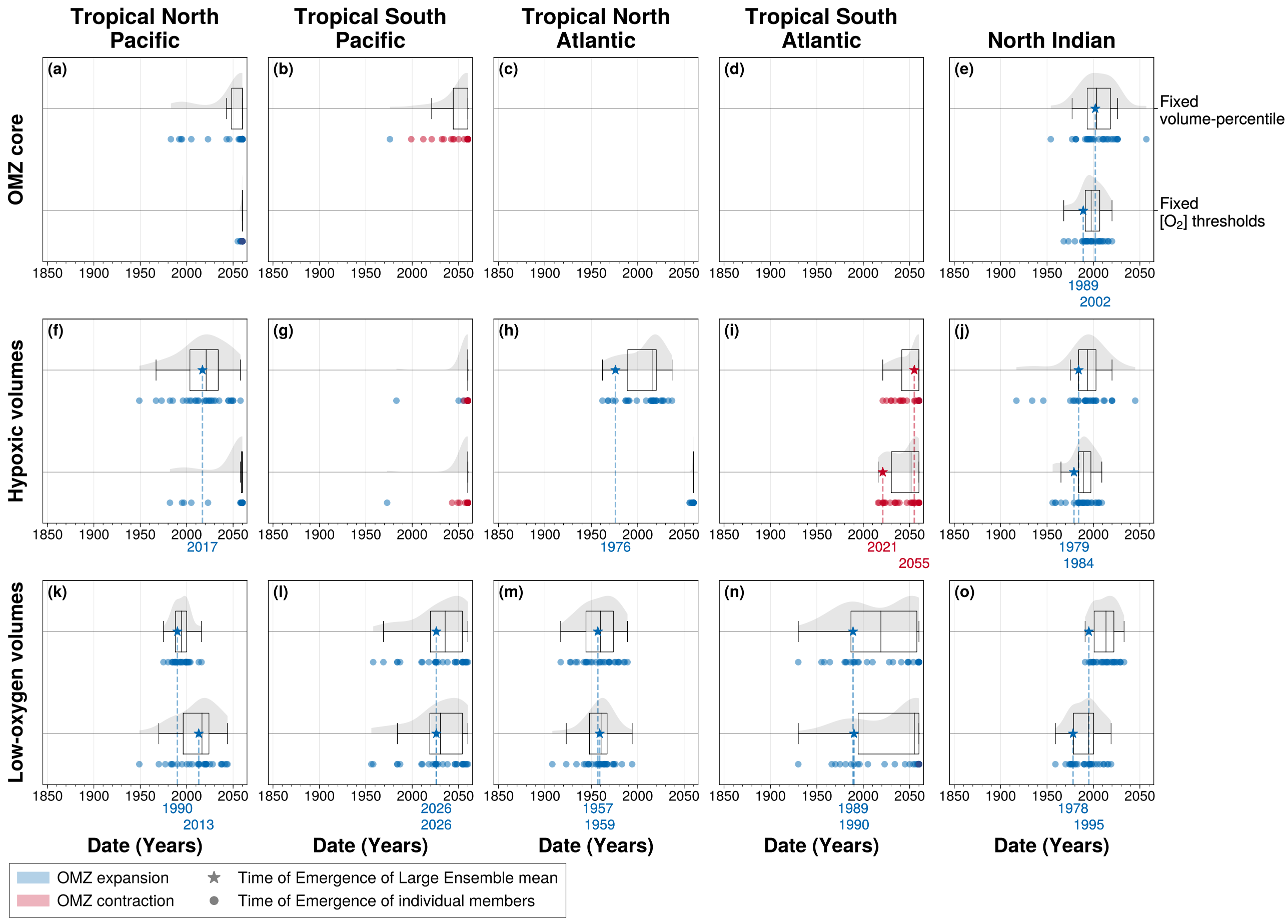

Figure A3. Time of emergence of OMZ volumes defined **(panels' first line)** in the ventilation-space with fixed volume-percentile versus **(panels' second line)** in the geographic-space with fixed dissolved oxygen concentration thresholds for **(columns)** each OMZ box. Times of emergence are computed for 100 – 1000m OMZ volume pre-industrial (1850-1900) anomalies for **(first row)** OMZ Core, **(second row)** Hypoxic volumes and **(third row)** Low-oxygen volumes. In all panels, the **box plots** illustrate the dispersion of the time of emergence around the median across the IPSL Large Ensemble, while the **violin plots** illustrate the distribution of the time of emergence within the IPSL Large Ensemble. The **star symbol** represents the time of emergence for the Large Ensemble mean when it exceeds the Large Ensemble standard deviation, while the **dots** represent the time of emergence for individual ensemble members signal when they exceed the piControl standard deviation. Their colours indicate the sign of their trend at the emergence: **blue** for deoxygenation or OMZ expansion, and **red** for oxygenation or OMZ contraction.

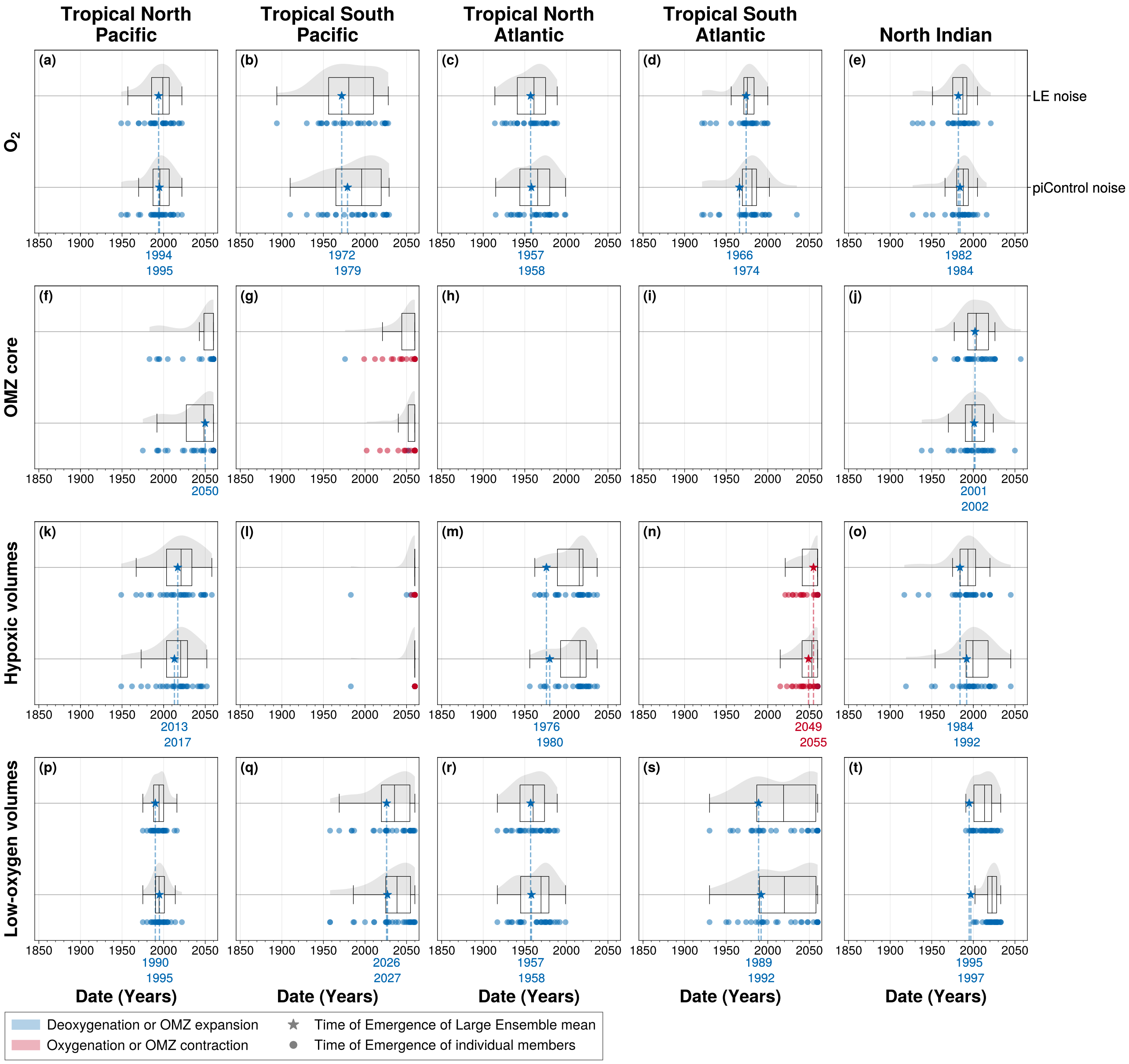

Figure A4. Time of emergence using for noise: **(panels' first line)** Large Ensemble inter-member standard deviation versus **(panels' second line)** piControl standard deviation. Times of emergence are computed, in **(columns)** each OMZ box, between 100 – 1000m, for **(first row)** spatial mean concentration anomalies of O_2 and OMZ volume anomalies for **(second row)** OMZ Core, **(third row)** Hypoxic volumes and **(fourth row)** Low-oxygen volumes. In all panels, the **box plots** illustrate the dispersion of the time of emergence around the median across the IPSL Large Ensemble, while the **violin plots** illustrate the distribution of the time of emergence within the IPSL Large Ensemble. The **star symbol** represents the time of emergence for the Large Ensemble mean when it exceeds the Large Ensemble standard deviation, while the **dots** represent the time of emergence for individual ensemble members signal when they exceed the piControl standard deviation. Their colours indicate the sign of their trend at the emergence: **blue** for deoxygenation or OMZ expansion, and **red** for oxygenation or OMZ contraction.

Code availability. This section needs to be completed. All codes necessary to reproduce the results in this manuscript will be made publicly available. Preliminary DOIs can be made available to the reviewers upon request.

Data availability. Publicly available datasets were analysed in this study. This data can be found at https://esgf.llnl.gov/ (Earth System Grid Federation , ESGF). The dissolved oxygen concentration data used in this study was downloaded from the World Ocean Atlas website (https://www.ncei.noaa.gov/products/world-ocean-atlas, García et al. (2018); World Ocean Atlas (WOA)) and Institute of Atmospheric Physics (IAP) from the Chinese Academy of Sciences http://dx.doi.org/10.12157/IOCAS.20231214.006 (Cheng and Gouretski, 2023).

Author contributions. M.L., L.B. and M.D. conceived the study. M.D. did the analysis and wrote the paper.

Competing interests. The contact author has declared that none of the authors has any competing interests.

Acknowledgements. We are grateful to the IPSL Large Ensemble Project. We acknowledge the support from the PPR Océan & Climat programme, jointly coordinated by CNRS and Ifremer and funded by the French government through the France 2030 investment plan, administered by the Agence Nationale pour la Recherche (ANR) under project number ANR-22-POCE-0001. This study benefitted from the ESPRI (Ensemble de Services Pour la Recherche à l'IPSL) computing and data centre (https://mesocentre.ipsl.fr/, last access: 14 May 2025), which is supported by CNRS, Sorbonne Université, École Polytechnique, and CNES and through national and international grants. We also thank Cosme Mosneron Dupin and Yona Silvy, whose comments and insights helped improve our study.

References

Aumont, O., Ethé, C., Tagliabue, A., Bopp, L., and Gehlen, M.: PISCES-v2: an ocean biogeochemical model for carbon and ecosystem studies, Geoscientific Model Development, 8, 2465–2513, https://doi.org/10.5194/gmd-8-2465-2015, 2015.

Bahl, A., Gnanadesikan, A., and Pradal, M.-A.: Variations in Ocean Deoxygenation Across Earth System Models: Isolating the Role of Parameterized Lateral Mixing, Global Biogeochemical Cycles, 33, 703–724, https://doi.org/10.1029/2018GB006121, 2019.

Bertrand, A., Chaigneau, A., Peraltilla, S., Ledesma, J., Graco, M., Monetti, F., and Chavez, F. P.: Oxygen: A Fundamental Property Regulating Pelagic Ecosystem Structure in the Coastal Southeastern Tropical Pacific, PLoS ONE, 6, e29 558, https://doi.org/10.1371/journal.pone.0029558, 2011.

Bonnet, R., Boucher, O., Deshayes, J., Gastineau, G., Hourdin, F., Mignot, J., Servonnat, J., and Swingedouw, D.: Presentation and Evaluation of the IPSL-CM6A-LR Ensemble of Extended Historical Simulations, Journal of Advances in Modeling Earth Systems, 13, e2021MS002 565, https://doi.org/10.1029/2021MS002565, 2021.

Bopp, L., Resplandy, L., Orr, J. C., Doney, S. C., Dunne, J. P., Gehlen, M., Halloran, P., Heinze, C., Ilyina, T., Séférian, R., Tjiputra, J., and Vichi, M.: Multiple stressors of ocean ecosystems in the 21st century: projections with CMIP5 models, Biogeosciences, 10, 6225–6245, https://doi.org/10.5194/bg-10-6225-2013, 2013.

Boucher, O., Servonnat, J., Albright, A. L., Aumont, O., Balkanski, Y., Bastrikov, V., Bekki, S., Bonnet, R., Bony, S., Bopp, L., Braconnot, P., Brockmann, P., Cadule, P., Caubel, A., Cheruy, F., Codron, F., Cozic, A., Cugnet, D., D'Andrea, F., Davini, P., de Lavergne, C., Denvil, S., Deshayes, J., Devilliers, M., Ducharne, A., Dufresne, J.-L., Dupont, E., Éthé, C., Fairhead, L., Falletti, L., Flavoni, S., Foujols, M.-A., Gardoll, S., Gastineau, G., Ghattas, J., Grandpeix, J.-Y., Guenet, B., Guez, E., L., Guilyardi, E., Guimberteau, M., Hauglustaine, D., Hourdin, F., Idelkadi, A., Joussaume, S., Kageyama, M., Khodri, M., Krinner, G., Lebas, N., Levavasseur, G., Lévy, C., Li, L., Lott, F., Lurton, T., Luyssaert, S., Madec, G., Madeleine, J.-B., Maignan, F., Marchand, M., Marti, O., Mellul, L., Meurdesoif, Y., Mignot, J., Musat, I., Ottlé, C., Peylin, P., Planton, Y., Polcher, J., Rio, C., Rochetin, N., Rousset, C., Sepulchre, P., Sima, A., Swingedouw, D., Thiéblemont, R., Traore, A. K., Vancoppenolle, M., Vial, J., Vialard, J., Viovy, N., and Vuichard, N.: Presentation and Evaluation of the IPSL-CM6A-LR Climate Model, Journal of Advances in Modeling Earth Systems, 12, e2019MS002 010, https://doi.org/10.1029/2019MS002010, 2020.

Busecke, J. J. M., Resplandy, L., Ditkovsky, S. J., and John, J. G.: Diverging Fates of the Pacific Ocean Oxygen Minimum Zone and Its Core in a Warming World, AGU Advances, 3, https://doi.org/10.1029/2021AV000470, 2022.

Cabré, A., Marinov, I., Bernardello, R., and Bianchi, D.: Oxygen minimum zones in the tropical Pacific across CMIP5 models: mean state differences and climate change trends, Biogeosciences, 12, 5429–5454, https://doi.org/10.5194/bg-12-5429-2015, 2015.

Cheng, L. and Gouretski, V.: IAP Global Ocean Oxygen gridded product (1-degree), https://doi.org/10.12157/IOCAS.20231214.006, 2023.

Cheng, L. and Zhu, J.: Benefits of CMIP5 Multimodel Ensemble in Reconstructing Historical Ocean Subsurface Temperature Variations, Journal of Climate, 29, 5393–5416, https://doi.org/10.1175/JCLI-D-15-0730.1, 2016.

Deser, C., Phillips, A., Bourdette, V., and Teng, H.: Uncertainty in climate change projections: the role of internal variability, Climate Dynamics, 38, 527–546, https://doi.org/10.1007/s00382-010-0977-x, 2012.

Deutsch, C., Berelson, W., Thunell, R., Weber, T., Tems, C., McManus, J., Crusius, J., Ito, T., Baumgartner, T., Ferreira, V., Mey, J., and Van Geen, A.: Centennial changes in North Pacific anoxia linked to tropical trade winds, Science, 345, 665–668, https://doi.org/10.1126/science.1252332, 2014.

Ditkovsky, S. and Resplandy, L.: Unifying Future Ocean Oxygen Projections Using an Oxygen Water Mass Framework, Journal of Geophysical Research: Oceans, 130, e2025JC022 333, https://doi.org/10.1029/2025JC022333, 2025.

Ditkovsky, S., Resplandy, L., and Busecke, J.: Unique ocean circulation pathways reshape the Indian Ocean oxygen minimum zone with warming, https://doi.org/10.5194/egusphere-2023-1082, 2023.

Dunne, J. P., Horowitz, L. W., Adcroft, A. J., Ginoux, P., Held, I. M., John, J. G., Krasting, J. P., Malyshev, S., Naik, V., Paulot, F., Shevliakova, E., Stock, C. A., Zadeh, N., Balaji, V., Blanton, C., Dunne, K. A., Dupuis, C., Durachta, J., Dussin, R., Gauthier, P. P. G., Griffies, S. M., Guo, H., Hallberg, R. W., Harrison, M., He, J., Hurlin, W., McHugh, C., Menzel, R., Milly, P. C. D., Nikonov, S., Paynter, D. J., Ploshay, J., Radhakrishnan, A., Rand, K., Reichl, B. G., Robinson, T., Schwarzkopf, D. M., Sentman, L. T., Underwood, S., Vahlenkamp, H., Winton, M., Wittenberg, A. T., Wyman, B., Zeng, Y., and Zhao, M.: The GFDL Earth System Model Version 4.1 (GFDL-ESM 4.1): Overall Coupled Model Description and Simulation Characteristics, Journal of Advances in Modeling Earth Systems, 12, e2019MS002 015, https://doi.org/10.1029/2019MS002015, 2020.

Duteil, O. and Oschlies, A.: Sensitivity of simulated extent and future evolution of marine suboxia to mixing intensity: SENSITIVITY OF SUBOXIA TO MIXING INTENSITY, Geophysical Research Letters, 38, n/a–n/a, https://doi.org/10.1029/2011GL046877, 2011.

Earth System Grid Federation (ESGF): https://esgf.llnl.gov/, last access: January 2025.

Eyring, V., Bony, S., Meehl, G. A., Senior, C. A., Stevens, B., Stouffer, R. J., and Taylor, K. E.: Overview of the Coupled Model Intercomparison Project Phase 6 (CMIP6) experimental design and organization, Geoscientific Model Development, 9, 1937–1958, https://doi.org/10.5194/gmd-9-1937-2016, 2016.

Firing, E., Filipe, Barna, A., and Abernathey, R.: TEOS-10/GSW-Python: v3.4.1.post0, https://doi.org/10.5281/zenodo.5214122, 2021.

Frankcombe, L. M., England, M. H., Mann, M. E., and Steinman, B. A.: Separating Internal Variability from the Externally Forced Climate Response, Journal of Climate, 28, 8184–8202, https://doi.org/10.1175/JCLI-D-15-0069.1, 2015.

García, H. E., Weathers, K. A., Paver, C. R., Smolyar, I. V., Boyer, T. P., Locarnini, R. A., Zweng, M. M., Mishonov, A. V., Baranova, O. K., Seidov, D., and Reagan, J. R.: World Ocean Atlas 2018, NOAA Atlas NESDIS 83, Volume 3: Dissolved Oxygen, Apparent Oxygen Utilization, and Dissolved Oxygen Saturation. A. Mishonov Technical Ed., 38pp, https://doi.org/10.25923/qspr-pn52, 2018.

Gnanadesikan, A., Russell, J. L., and Zeng, F.: How does ocean ventilation change under global warming?, Ocean Science, 3, 43–53, https://doi.org/10.5194/os-3-43-2007, 2007.

Gnanadesikan, A., Dunne, J. P., and John, J.: Understanding why the volume of suboxic waters does not increase over centuries of global warming in an Earth System Model, Biogeosciences, 9, 1159–1172, https://doi.org/10.5194/bg-9-1159-2012, 2012.

Gong, H., Li, C., and Zhou, Y.: Emerging Global Ocean Deoxygenation Across the 21st Century, Geophysical Research Letters, 48, e2021GL095 370, https://doi.org/10.1029/2021GL095370, 2021.

Gouretski, V., Cheng, L., Du, J., Xing, X., Chai, F., and Tan, Z.: A consistent ocean oxygen profile dataset with new quality control and bias assessment, Earth System Science Data, 16, 5503–5530, https://doi.org/10.5194/essd-16-5503-2024, 2024.

Gupta, A. S., Jourdain, N. C., Brown, J. N., and Monselesan, D.: Climate Drift in the CMIP5 Models*, Journal of Climate, 26, 8597–8615, https://doi.org/10.1175/JCLI-D-12-00521.1, 2013.

Hajima, T., Watanabe, M., Yamamoto, A., Tatebe, H., Noguchi, M. A., Abe, M., Ohgaito, R., Ito, A., Yamazaki, D., Okajima, H., Ito, A., Takata, K., Ogochi, K., Watanabe, S., and Kawamiya, M.: Development of the MIROC-ES2L Earth system model and the evaluation of biogeochemical processes and feedbacks, Geoscientific Model Development, 13, 2197–2244, https://doi.org/10.5194/gmd-13-2197-2020, 2020.

Hameau, A., Mignot, J., and Joos, F.: Assessment of time of emergence of anthropogenic deoxygenation and warming: insights from a CESM simulation from 850 to 2100 CE, Biogeosciences, 16, 1755–1780, https://doi.org/10.5194/bg-16-1755-2019, 2019.

https://doi.org/10.5194/egusphere-2025-2805
Preprint. Discussion started: 23 July 2025

Hameau, A., Frölicher, T. L., Mignot, J., and Joos, F.: Is deoxygenation detectable before warming in the thermocline?, Biogeosciences, 17, 1877–1895, https://doi.org/10.5194/bg-17-1877-2020, 2020.

Hasselmann, K.: Stochastic climate models: Part I. Theory, Tellus A: Dynamic Meteorology and Oceanography, 28, 473, https://doi.org/10.3402/tellusa.v28i6.11316, 1976.

Hasselmann, K.: Optimal Fingerprints for the Detection of Time-dependent Climate Change, Journal of Climate, 6, 1957–1971, https://doi.org/10.1175/1520-0442(1993)006<1957:OFFTDO>2.0.CO;2, 1993.

Hawkins, E. and Sutton, R.: Time of emergence of climate signals, Geophysical Research Letters, 39, https://doi.org/10.1029/2011GL050087, 2012.

Held, I. M., Guo, H., Adcroft, A., Dunne, J. P., Horowitz, L. W., Krasting, J., Shevliakova, E., Winton, M., Zhao, M., Bushuk, M., Wittenberg, A. T., Wyman, B., Xiang, B., Zhang, R., Anderson, W., Balaji, V., Donner, L., Dunne, K., Durachta, J., Gauthier, P. P. G., Ginoux, P., Golaz, J., Griffies, S. M., Hallberg, R., Harris, L., Harrison, M., Hurlin, W., John, J., Lin, P., Lin, S., Malyshev, S., Menzel, R., Milly, P. C. D., Ming, Y., Naik, V., Paynter, D., Paulot, F., Ramaswamy, V., Reichl, B., Robinson, T., Rosati, A., Seman, C., Silvers, L. G., Underwood, S., and Zadeh, N.: Structure and Performance of GFDL's CM4.0 Climate Model, Journal of Advances in Modeling Earth Systems, 11, 3691–3727, https://doi.org/10.1029/2019MS001829, 2019.

Hourdin, F., Rio, C., Grandpeix, J., Madeleine, J., Cheruy, F., Rochetin, N., Jam, A., Musat, I., Idelkadi, A., Fairhead, L., Foujols, M., Mellul, L., Traore, A., Dufresne, J., Boucher, O., Lefebvre, M., Millour, E., Vignon, E., Jouhaud, J., Diallo, F. B., Lott, F., Gastineau, G., Caubel, A., Meurdesoif, Y., and Ghattas, J.: LMDZ6A: The Atmospheric Component of the IPSL Climate Model With Improved and Better Tuned Physics, Journal of Advances in Modeling Earth Systems, 12, e2019MS001 892, https://doi.org/10.1029/2019MS001892, 2020.

Ito, T. and Deutsch, C.: A conceptual model for the temporal spectrum of oceanic oxygen variability, Geophysical Research Letters, 37, 2009GL041 595, https://doi.org/10.1029/2009GL041595, 2010.

Ito, T., Minobe, S., Long, M. C., and Deutsch, C.: Upper ocean O 2 trends: 1958–2015, Geophysical Research Letters, 44, 4214–4223, https://doi.org/10.1002/2017GL073613, 2017.

Ji, Q., Babbin, A. R., Jayakumar, A., Oleynik, S., and Ward, B. B.: Nitrous oxide production by nitrification and denitrification in the Eastern Tropical South Pacific oxygen minimum zone, Geophysical Research Letters, 42, https://doi.org/10.1002/2015GL066853, 2015.

Kay, J. E., Deser, C., Phillips, A., Mai, A., Hannay, C., Strand, G., Arblaster, J. M., Bates, S. C., Danabasoglu, G., Edwards, J., Holland, M., Kushner, P., Lamarque, J.-F., Lawrence, D., Lindsay, K., Middleton, A., Munoz, E., Neale, R., Oleson, K., Polvani, L., and Vertenstein, M.: The Community Earth System Model (CESM) Large Ensemble Project: A Community Resource for Studying Climate Change in the Presence of Internal Climate Variability, Bulletin of the American Meteorological Society, 96, 1333–1349, https://doi.org/10.1175/BAMS-D-13-00255.1, 2015.

Keeling, R. F., Körtzinger, A., and Gruber, N.: Ocean Deoxygenation in a Warming World, Annual Review of Marine Science, 2, 199–229, https://doi.org/10.1146/annurev.marine.010908.163855, 2010.

Krinner, G., Viovy, N., De Noblet-Ducoudré, N., Ogée, J., Polcher, J., Friedlingstein, P., Ciais, P., Sitch, S., and Prentice, I. C.: A dynamic global vegetation model for studies of the coupled atmosphere-biosphere system, Global Biogeochemical Cycles, 19, 2003GB002 199, https://doi.org/10.1029/2003GB002199, 2005.

Kwiatkowski, L., Torres, O., Bopp, L., Aumont, O., Chamberlain, M., Christian, J. R., Dunne, J. P., Gehlen, M., Ilyina, T., John, J. G., Lenton, A., Li, H., Lovenduski, N. S., Orr, J. C., Palmieri, J., Santana-Falcón, Y., Schwinger, J., Séférian, R., Stock, C. A., Tagliabue, A., Takano, Y., Tjiputra, J., Toyama, K., Tsujino, H., Watanabe, M., Yamamoto, A., Yool, A., and Ziehn, T.: Twenty-first century ocean warming, acidification, deoxygenation, and upper-ocean nutrient and primary production decline from CMIP6 model projections, Biogeosciences, 17, 3439–3470, https://doi.org/10.5194/bg-17-3439-2020, 2020.

Levin, L. A.: Manifestation, Drivers, and Emergence of Open Ocean Deoxygenation, Annual Review of Marine Science, 10, 229–260, https://doi.org/10.1146/annurev-marine-121916-063359, 2018.

Long, M. C., Deutsch, C., and Ito, T.: Finding forced trends in oceanic oxygen, Global Biogeochemical Cycles, 30, 381–397, https://doi.org/10.1002/2015GB005310, 2016.

Lorenz, E. N.: Deterministic Nonperiodic Flow, Journal of the Atmospheric Sciences, 20, 130–141, https://doi.org/10.1175/1520-0469(1963)020<0130:DNF>2.0.CO;2, 1963.

Luyten, J. R., Pedlosky, J., and Stommel, H.: The Ventilated Thermocline, Journal of Physical Oceanography, 13, 292–309, https://doi.org/10.1175/1520-0485(1983)013<0292:TVT>2.0.CO;2, 1983.

Lévy, M., Resplandy, L., Palter, J. B., Couespel, D., and Lachkar, Z.: The crucial contribution of mixing to present and future ocean oxygen distribution, p. 329–344, Elsevier, ISBN 978-0-12-821512-8, https://doi.org/10.1016/B978-0-12-821512-8.00020-7, 2022.

Madec, G., Bourdallé-Badie, R., Bouttier, P.-A., Bricaud, C., Bruciaferri, D., Calvert, D., Chanut, J., Clementi, E., Coward, A., Delrosso, D., Ethé, C., Flavoni, S., Graham, T., Harle, J., Iovino, D., Lea, D., Lévy, C., Lovato, T., Martin, N., Masson, S., Mocavero, S., Paul, J., Rousset, C., Storkey, D., Storto, A., and Vancoppenolle, M.: NEMO ocean engine, https://doi.org/10.5281/zenodo.3248739, citation Key: madecNEMOOceanEngine2017, 2017.

Mann, M. E.: Smoothing of climate time series revisited, Geophysical Research Letters, 35, 2008GL034 716, https://doi.org/10.1029/2008GL034716, 2008.

Mauritsen, T., Bader, J., Becker, T., Behrens, J., Bittner, M., Brokopf, R., Brovkin, V., Claussen, M., Crueger, T., Esch, M., Fast, I., Fiedler, S., Fläschner, D., Gayler, V., Giorgetta, M., Goll, D. S., Haak, H., Hagemann, S., Hedemann, C., Hohenegger, C., Ilyina, T., Jahns, T., Jimenéz-de-la-Cuesta, D., Jungclaus, J., Kleinen, T., Kloster, S., Kracher, D., Kinne, S., Kleberg, D., Lasslop, G., Kornblueh, L., Marotzke, J., Matei, D., Meraner, K., Mikolajewicz, U., Modali, K., Möbis, B., Müller, W. A., Nabel, J. E. M. S., Nam, C. C. W., Notz, D., Nyawira, S., Paulsen, H., Peters, K., Pincus, R., Pohlmann, H., Pongratz, J., Popp, M., Raddatz, T. J., Rast, S., Redler, R., Reick, C. H., Rohrschneider, T., Schemann, V., Schmidt, H., Schnur, R., Schulzweida, U., Six, K. D., Stein, L., Stemmler, I., Stevens, B., Von Storch, J., Tian, F., Voigt, A., Vrese, P., Wieners, K., Wilkenskjeld, S., Winkler, A., and Roeckner, E.: Developments in the MPI-M Earth System Model version 1.2 (MPI-ESM1.2) and Its Response to Increasing CO2, Journal of Advances in Modeling Earth Systems, 11, 998–1038, https://doi.org/10.1029/2018MS001400, 2019.

Mignot, J., Hourdin, F., Deshayes, J., Boucher, O., Gastineau, G., Musat, I., Vancoppenolle, M., Servonnat, J., Caubel, A., Chéruy, F., Denvil, S., Dufresne, J., Ethé, C., Fairhead, L., Foujols, M., Grandpeix, J., Levavasseur, G., Marti, O., Menary, M., Rio, C., Rousset, C., and Silvy, Y.: The Tuning Strategy of IPSL-CM6A-LR, Journal of Advances in Modeling Earth Systems, 13, e2020MS002 340, https://doi.org/10.1029/2020MS002340, 2021.

Miller, D., Poucher, S., and Coiro, L.: Determination of lethal dissolved oxygen levels for selected marine and estuarine fishes, crustaceans, and a bivalve, Marine Biology, 140, 287–296, https://doi.org/10.1007/s002270100702, 2002.

Moss, R. H., Edmonds, J. A., Hibbard, K. A., Manning, M. R., Rose, S. K., Van Vuuren, D. P., Carter, T. R., Emori, S., Kainuma, M., Kram, T., Meehl, G. A., Mitchell, J. F. B., Nakicenovic, N., Riahi, K., Smith, S. J., Stouffer, R. J., Thomson, A. M., Weyant, J. P., and Wilbanks, T. J.: The next generation of scenarios for climate change research and assessment, Nature, 463, 747–756, https://doi.org/10.1038/nature08823, 2010.

https://doi.org/10.5194/egusphere-2025-2805
Preprint. Discussion started: 23 July 2025

Müller, W. A., Jungclaus, J. H., Mauritsen, T., Baehr, J., Bittner, M., Budich, R., Bunzel, F., Esch, M., Ghosh, R., Haak, H., Ilyina, T., Kleine, T., Kornblueh, L., Li, H., Modali, K., Notz, D., Pohlmann, H., Roeckner, E., Stemmler, I., Tian, F., and Marotzke, J.: A Higher-resolution Version of the Max Planck Institute Earth System Model (MPI-ESM1.2-HR), Journal of Advances in Modeling Earth Systems, 10, 1383–1413, https://doi.org/10.1029/2017MS001217, 2018.

O'Neill, B. C., Tebaldi, C., Van Vuuren, D. P., Eyring, V., Friedlingstein, P., Hurtt, G., Knutti, R., Kriegler, E., Lamarque, J.-F., Lowe, J., Meehl, G. A., Moss, R., Riahi, K., and Sanderson, B. M.: The Scenario Model Intercomparison Project (ScenarioMIP) for CMIP6, Geoscientific Model Development, 9, 3461–3482, https://doi.org/10.5194/gmd-9-3461-2016, 2016.

Paulmier, A. and Ruiz-Pino, D.: Oxygen minimum zones (OMZs) in the modern ocean, Progress in Oceanography, 80, 113–128, https://doi.org/10.1016/j.pocean.2008.08.001, 2009.

Poupon, M. A., Resplandy, L., Lévy, M., and Bopp, L.: Pacific Decadal Oscillation Influences Tropical Oxygen Minimum Zone Extent and Obscures Anthropogenic Changes, Geophysical Research Letters, 50, e2022GL102 123, https://doi.org/10.1029/2022GL102123, 2023.

Resplandy, L.: Will ocean zones with low oxygen levels expand or shrink?, Nature, p. 315, https://doi.org/10.1038/d41586-018-05034-y, 2018.

Rousset, C., Vancoppenolle, M., Madec, G., Fichefet, T., Flavoni, S., Barthélemy, A., Benshila, R., Chanut, J., Levy, C., Masson, S., and Vivier, F.: The Louvain-La-Neuve sea ice model LIM3.6: global and regional capabilities, Geoscientific Model Development, 8, 2991–3005, https://doi.org/10.5194/gmd-8-2991-2015, 2015.

Santer, B. D., Brüggemann, W., Cubasch, U., Hasselmann, K., Höck, H., Maier-Reimer, E., and Mikolajewica, U.: Signal-to-noise analysis of time-dependent greenhouse warming experiments: Part 1: pattern analysis, Climate Dynamics, 9, 267–285, https://doi.org/10.1007/BF00204743, 1994.

Schmidt, H., Getzlaff, J., Löptien, U., and Oschlies, A.: Causes of uncertainties in the representation of the Arabian Sea oxygen minimum zone in CMIP5 models, Ocean Science, 17, 1303–1320, https://doi.org/10.5194/os-17-1303-2021, 2021.

Schmidtko, S., Stramma, L., and Visbeck, M.: Decline in global oceanic oxygen content during the past five decades, Nature, 542, 335–339, https://doi.org/10.1038/nature21399, 2017.

Sellar, A. A., Jones, C. G., Mulcahy, J. P., Tang, Y., Yool, A., Wiltshire, A., O'Connor, F. M., Stringer, M., Hill, R., Palmieri, J., Woodward, S., De Mora, L., Kuhlbrodt, T., Rumbold, S. T., Kelley, D. I., Ellis, R., Johnson, C. E., Walton, J., Abraham, N. L., Andrews, M. B., Andrews, T., Archibald, A. T., Berthou, S., Burke, E., Blockley, E., Carslaw, K., Dalvi, M., Edwards, J., Folberth, G. A., Gedney, N., Griffiths, P. T., Harper, A. B., Hendry, M. A., Hewitt, A. J., Johnson, B., Jones, A., Jones, C. D., Keeble, J., Liddicoat, S., Morgenstern, O., Parker, R. J., Predoi, V., Robertson, E., Siahaan, A., Smith, R. S., Swaminathan, R., Woodhouse, M. T., Zeng, G., and Zerroukat, M.: UKESM1: Description and Evaluation of the U.K. Earth System Model, Journal of Advances in Modeling Earth Systems, 11, 4513–4558, https://doi.org/10.1029/2019MS001739, 2019.

Silvy, Y., Sallée, J.-B., Guilyardi, E., Mignot, J., and Rousset, C.: What Causes Anthropogenic Ocean Warming to Emerge from Internal Variability in a Coupled Model?, Journal of Climate, 35, 7435–7454, https://doi.org/10.1175/JCLI-D-22-0074.1, 2022.

Sohail, T., Irving, D. B., Zika, J. D., Holmes, R. M., and Church, J. A.: Fifty Year Trends in Global Ocean Heat Content Traced to Surface Heat Fluxes in the Sub-Polar Ocean, Geophysical Research Letters, 48, e2020GL091 439, https://doi.org/10.1029/2020GL091439, 2021.

Stock, C. A., Dunne, J. P., Fan, S., Ginoux, P., John, J., Krasting, J. P., Laufkötter, C., Paulot, F., and Zadeh, N.: Ocean Biogeochemistry in GFDL's Earth System Model 4.1 and Its Response to Increasing Atmospheric CO2, Journal of Advances in Modeling Earth Systems, 12, e2019MS002 043, https://doi.org/10.1029/2019MS002043, 2020.

https://doi.org/10.5194/egusphere-2025-2805
Preprint. Discussion started: 23 July 2025

Storch, H. v. and Swiers, F. W.: Statistical analysis in climate research, Cambridge university press, Cambridge, ISBN 978-0-521-45071-3, 1999.

Stramma, L., Johnson, G. C., Sprintall, J., and Mohrholz, V.: Expanding Oxygen-Minimum Zones in the Tropical Oceans, Science, 320, 655–658, https://doi.org/10.1126/science.1153847, 2008.

Stramma, L., Prince, E. D., Schmidtko, S., Luo, J., Hoolihan, J. P., Visbeck, M., Wallace, D. W. R., Brandt, P., and Körtzinger, A.: Expansion of oxygen minimum zones may reduce available habitat for tropical pelagic fishes, Nature Climate Change, 2, 33–37, https://doi.org/10.1038/nclimate1304, 2012.

Swart, N. C., Cole, J. N. S., Kharin, V. V., Lazare, M., Scinocca, J. F., Gillett, N. P., Anstey, J., Arora, V., Christian, J. R., Hanna, S., Jiao, Y., Lee, W. G., Majaess, F., Saenko, O. A., Seiler, C., Seinen, C., Shao, A., Sigmond, M., Solheim, L., von Salzen, K., Yang, D., and Winter, B.: The Canadian Earth System Model version 5 (CanESM5.0.3), Geoscientific Model Development, 12, 4823–4873, https://doi.org/10.5194/gmd-12-4823-2019, 2019.

Séférian, R., Nabat, P., Michou, M., Saint-Martin, D., Voldoire, A., Colin, J., Decharme, B., Delire, C., Berthet, S., Chevallier, M., Sénési, S., Franchisteguy, L., Vial, J., Mallet, M., Joetzjer, E., Geoffroy, O., Guérémy, J., Moine, M., Msadek, R., Ribes, A., Rocher, M., Roehrig, R., Salas-y-Mélia, D., Sanchez, E., Terray, L., Valcke, S., Waldman, R., Aumont, O., Bopp, L., Deshayes, J., Éthé, C., and Madec, G.: Evaluation of CNRM Earth System Model, CNRM-ESM2-1: Role of Earth System Processes in Present-Day and Future Climate, Journal of Advances in Modeling Earth Systems, 11, 4182–4227, https://doi.org/10.1029/2019MS001791, 2019.

Takano, Y., Ilyina, T., Tjiputra, J., Eddebbar, Y., Berthet, S., Bopp, L., Buitenhuis, E., Butenschön, M., Christian, J. R., Dunne, J. P., Gröger, M., Hayashida, H., Hieronymus, J., Koenigk, T., Krasting, J. P., Long, M. C., Lovato, T., Nakano, H., Palmieri, J., Schwinger, J., Séférian, R., Suntharalingam, P., Tatebe, H., Tsujino, H., Urakawa, S., Watanabe, M., and Yool, A.: Simulations of ocean deoxygenation in the historical era: insights from forced and coupled models, Frontiers in Marine Science, 10, 1139 917, https://doi.org/10.3389/fmars.2023.1139917, 2023.

Taylor, K. E., Stouffer, R. J., and Meehl, G. A.: An Overview of CMIP5 and the Experiment Design, Bulletin of the American Meteorological Society, 93, 485–498, https://doi.org/10.1175/BAMS-D-11-00094.1, 2012.

Tjiputra, J. F., Schwinger, J., Bentsen, M., Morée, A. L., Gao, S., Bethke, I., Heinze, C., Goris, N., Gupta, A., He, Y.-C., Olivié, D., Seland, O., and Schulz, M.: Ocean biogeochemistry in the Norwegian Earth System Model version 2 (NorESM2), Geoscientific Model Development, 13, 2393–2431, https://doi.org/10.5194/gmd-13-2393-2020, 2020.

Vancoppenolle, M., Fichefet, T., and Goosse, H.: Simulating the mass balance and salinity of Arctic and Antarctic sea ice. 2. Importance of sea ice salinity variations, Ocean Modelling, 27, 54–69, https://doi.org/10.1016/j.ocemod.2008.11.003, 2009.

Vaquer-Sunyer, R. and Duarte, C. M.: Thresholds of hypoxia for marine biodiversity, Proceedings of the National Academy of Sciences, 105, 15 452–15 457, https://doi.org/10.1073/pnas.0803833105, 2008.

World Ocean Atlas (WOA): https://www.ncei.noaa.gov/products/world-ocean-atlas, last access: January 2025.

Yukimoto, S., Kawai, H., Koshiro, T., Oshima, N., Yoshida, K., Urakawa, S., Tsujino, H., Deushi, M., Tanaka, T., Hosaka, M., Yabu, S., Yoshimura, H., Shindo, E., Mizuta, R., Obata, A., Adachi, Y., and Ishii, M.: The Meteorological Research Institute Earth System Model Version 2.0, MRI-ESM2.0: Description and Basic Evaluation of the Physical Component, Journal of the Meteorological Society of Japan. Ser. II, 97, 931–965, https://doi.org/10.2151/jmsj.2019-051, 2019.

Ziehn, T., Chamberlain, M. A., Law, R. M., Lenton, A., Bodman, R. W., Dix, M., Stevens, L., Wang, Y.-P., and Srbinovsky, J.: The Australian Earth System Model: ACCESS-ESM1.5, Journal of Southern Hemisphere Earth Systems Science, 70, 193–214, https://doi.org/10.1071/ES19035, 2020.